

Attosecond X-ray Chronoscopy of Core-level Photoemission

Jia-Bao Ji,^{1*} Zhaoheng Guo,^{2,3,4*} Taran Driver,^{2,3} Cynthia S. Trevisan,⁵,
David Cesar,² Xinxin Cheng,² Joseph Duris,² Paris L. Franz,^{2,3} James Glowonia,²
Xiaochun Gong,^{1,6} Daniel Hammerland,¹ Meng Han,^{1,7} Saijoscha Heck,¹
Matthias Hoffmann,² Andrei Kamalov,² Kirk A. Larsen,^{2,3} Xiang Li,²
Ming-Fu Lin,² Yuchen Liu,^{8,9} C. William McCurdy,^{8,9} Razib Obaid,²
Jordan T. O'Neal,³ Thomas N. Rescigno,⁸ River R. Robles,^{2,3} Nicholas Sudar,^{2,3}
Peter Walter,² Anna L. Wang,^{2,3} Jun Wang,^{2,3} Thomas J. A. Wolf,^{2,3} Zhen Zhang,²
Kiyoshi Ueda,^{1,10,11} Robert R. Lucchese,^{8†} Agostino Marinelli,^{2,3†}
James P. Cryan,^{2,3†} Hans Jakob Wörner^{1†}

¹Laboratory of Physical Chemistry, ETH Zürich, Zurich, Switzerland

²SLAC National Accelerator Laboratory, Menlo Park, CA, USA

³Stanford PULSE Institute, SLAC National Accelerator Laboratory, Menlo Park, CA, USA

⁴Laboratory for Ultrafast X-ray Sciences, EPFL, Lausanne, Switzerland

⁵California State University, Maritime Academy, Vallejo, CA, USA

⁶State Key Laboratory of Extreme Photonics and Instrumentation,
College of Optical Science and Engineering, Zhejiang University, Hangzhou 310058, China

⁷J. R. Macdonald Laboratory, Department of Physics, Kansas State University, Manhattan, KS, USA

⁸Lawrence Berkeley National Laboratory, Berkeley, CA, USA

⁹Department of Chemistry, University of California, Davis, CA, USA

¹⁰Department of Chemistry, Tohoku University, Sendai, Japan

¹¹School of Physical Science and Technology, ShanghaiTech University, Shanghai, China

*These authors contributed equally.

†To whom correspondence should be addressed;

E-mail: rlucchese@lbl.gov, marinelli@slac.stanford.edu, jcryan@stanford.edu,
hwoerner@ethz.ch.

Attosecond photoemission or photoionization delays are a unique probe of the structure and the electronic dynamics of matter. However, spectral congestion and spatial delocalization of valence electron wave functions set fundamental limits to the complexity of systems that can be studied and the information that can be retrieved, respectively. Using attosecond X-ray pulses from LCLS, we demonstrate the key advantages of measuring core-level delays: the photoelectron spectra remain atom-like, the measurements become element specific and the observed scattering dynamics originate from a point-like source. We exploit these unique features to reveal the effects of electronegativity and symmetry on attosecond scattering dynamics by measuring the photoionization delays between N-1s and C-1s core shells of a series of aromatic azabenzene molecules. Remarkably, the delays systematically increase with the number of nitrogen atoms in the molecule and reveal multiple resonances. We identify two previously unknown mechanisms regulating the associated attosecond dynamics, namely the enhanced confinement of the trapped wavefunction with increasing electronegativity of the atoms and the decrease of the coupling strength among the photoemitted partial waves with increasing symmetry. This study demonstrates the unique opportunities opened by measurements of core-level photoionization delays for unravelling attosecond electron dynamics in complex matter.

Tracking attosecond multi-electron dynamics with atomically resolved spatial information is the current focus of numerous research efforts worldwide. X-ray spectroscopy has established itself as a powerful solution to breaking the complexity barriers faced by valence-shell spectroscopies. These barriers are particularly noticeable in time-resolved studies of the photoelectric effect, known as attosecond chronoscopy (1–3). This technique has integrated time-domain access to multi-electron dynamics into the powerful framework of electron-scattering physics which has created a flourishing research field with applications to molecules (4–9), clusters (10, 11), liquids (12) and solids (13–16). Such studies have traditionally made use of attosecond pulses in the extreme ultraviolet (up to 120 eV), which has so far prevented access to atomic core levels.

Here, we demonstrate the unique opportunities that arise from advancing the research field of attosecond chronoscopy from the extreme-ultraviolet to the X-ray domain. This adds element specificity and site selectivity to the method, while simultaneously confining the emission site of the photoelectron wave to a point-like source. Moreover, core-shell photoelectron spectra have a much simpler structure than valence-shell spectra because they feature a single band per atom of each type (when neglecting satellite lines), which facilitates the extension of the method to complex forms of matter. This advance was made possible by groundbreaking progress in free-electron-laser (FEL) science that has led to the generation of attosecond pulses in the X-ray domain through the XLEAP technique (17). The long-standing challenge of temporal jitter between the FEL pulses and laser pulses was solved by using attosecond angular streaking with a circularly-polarized infrared laser pulse and detecting the photoelectron momentum distribution in the polarization plane (18, 19).

The present experiments establish the unique capabilities of X-ray chronoscopy at unraveling the mechanisms of attosecond electron dynamics in complex systems, notably in aromatic molecules (i.e., benzene derivatives). Specifically, our study reveals the multiple-scattering phenomena that lead to transient trapping of photoelectrons following their release from specific atoms. Our results reveal two previously unknown mechanisms regulating such attosecond scattering dynamics. First, we find that substituting the ionized functional group with a more electronegative one (C-H \rightarrow N) increases the trapping times. Second, we show that increasing the symmetry of the molecular scaffold also increases the trapping times by suppressing the coupling to the less-trapped partial waves with lower angular momentum. To demonstrate these effects, we chose the azabenzene molecules pyridine, pyrimidine and *s*-triazine, depicted in Fig. 1A. We produced attosecond X-ray pulses with energies just above the nitrogen K-edge located

at ~ 405 eV and measured the photoionization delays between the electrons emitted from the nitrogen K -shell (N-1s) and those emitted from the carbon K -shell (C-1s). Since the latter have kinetic energies of more than 110 eV, the C-1s electrons are emitted with negligible photoionization delays ($\lesssim 5$ as), defining a self-referenced technique for accessing absolute photoionization delays of the N-1s electrons. We measured N-1s photoionization delays of up to ~ 300 as close to the nitrogen K -shell threshold, which generally decrease with increasing kinetic energy but display local maxima at 3-15 eV above the threshold. The measured delays also markedly increase from pyridine to pyrimidine and s -triazine. These experimental results are compared with state-of-the-art core-level photoionization calculations, which reveal the presence of several shape resonances in this low kinetic-energy region. The comparison of experiment and theory reveals that the photoelectrons originating from the nitrogen K -shell are trapped with increasing efficiency in the molecular plane in the sequence pyridine, pyrimidine, s -triazine, i.e., with increasing number of nitrogen atoms. Additionally, the increasing symmetry of the molecular scaffold (from C_{2v} in pyridine to D_{3h} in s -triazine) reduces the coupling among the photoelectron partial waves, which frustrates the decay of the trapped partial waves with high angular momentum. Pyrimidine is a building block of the nucleobases thymine, cytosine and uracil. All three azabenzene molecules are widespread structural motifs in biomolecules, drugs and molecular optoelectronics (20–23). The discovered mechanisms therefore suggest guidelines for understanding electronic dynamics in biomolecules and molecular optoelectronics.

Figure 1 illustrates the principle of the present experiments, carried out at the time-resolved atomic, molecular, and optical science (TMO) experimental hutch (24) of the Linac Coherent Light Source (LCLS). Linearly polarized attosecond X-ray pulses with a tunable central energy were obtained using the XLEAP technique (17) and were superimposed with circularly polarized short-wave infrared (IR, $1.3 \mu\text{m}$, ~ 40 fs) pulses in the interaction region of a co-axial velocity-map-imaging (c-VMI) spectrometer. A continuous molecular beam containing pyridine, pyrimidine or s -triazine intersected with the overlapping X-ray and IR pulses in the interaction region. The photoelectrons created from nitrogen K -shell ionization of the sample were streaked by the IR pulses and projected onto a position-sensitive imaging detector with a central hole. A photoelectron image recorded by ionizing pyrimidine with X-ray pulses centered at 454 eV is shown in Fig. 1A, whereby the inner (outer) ring corresponds to ionization of the nitrogen (carbon) K -shell electrons. Figures 1B, 1C, and 1D show how the relative photoionization delays between the N-1s and C-1s photoelectrons were determined. Because each photoelectron was angularly streaked into the direction of the IR-laser vector potential at the instant of

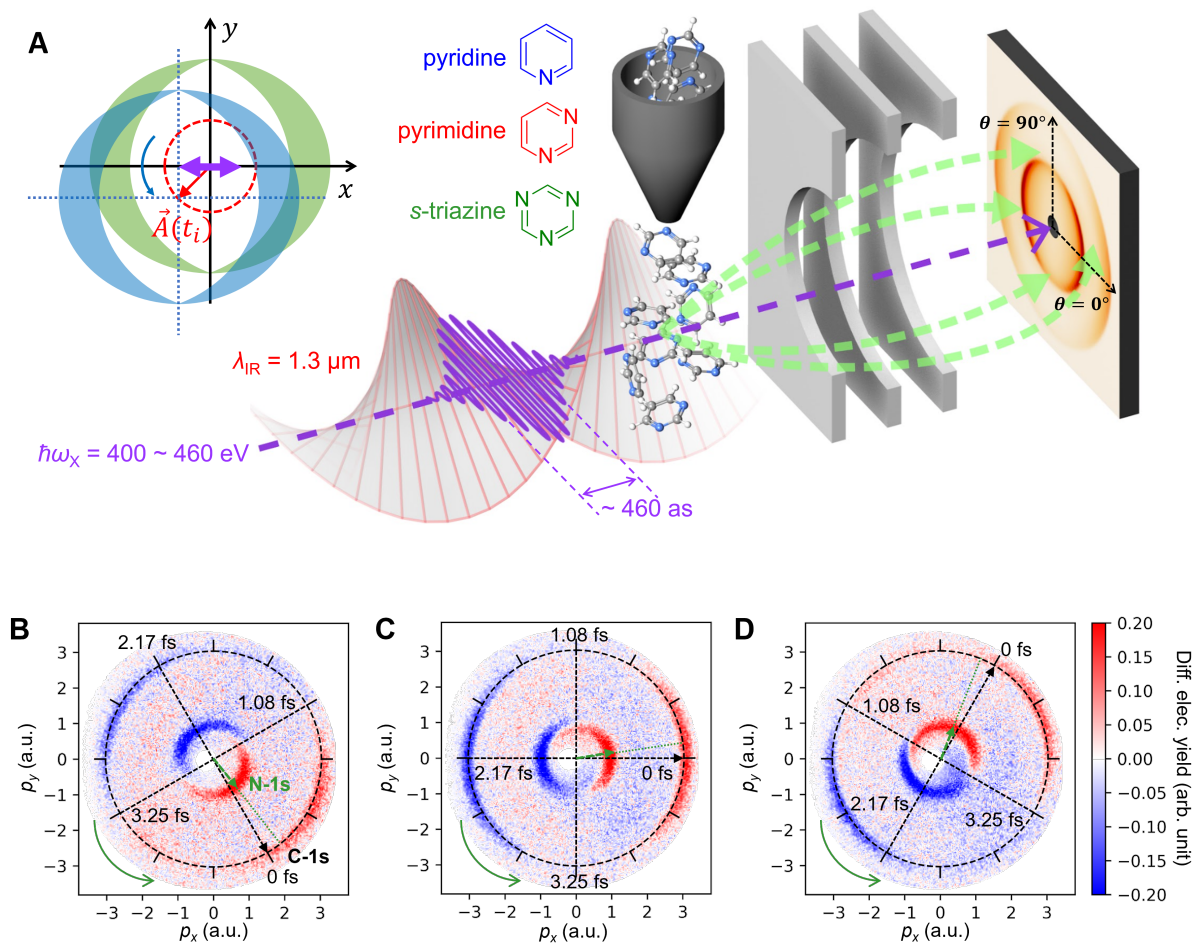


Figure 1: The principle of measuring core-level photoionization delays with an XFEL. (A) Gas-phase azabenzene molecules (pyridine, pyrimidine or *s*-triazine) are ionized by the attosecond X-ray Free-Electron Laser (XFEL) pulses in the presence of a $1.3 \mu\text{m}$ circularly polarized streaking laser field. The photoelectrons are collected with a co-axial velocity-mapping (c-VMI) spectrometer, with θ as the polar angle on the detector. The top-left inset illustrates how the initial photoelectron momentum distribution (green) is shifted by the vector potential of the IR field $\vec{A}(t_i)$ at the instant of ionization t_i , where the purple double arrow indicates the X-ray polarization direction. (B,C,D) Difference images between streaking within a narrow range of angles and the average over all streaking angles, revealing the angular offset of the N-1s and C-1s electrons, which directly encodes their time delay.

photoionization (inset of Fig.1A), the relative streaking angle between N-1s and C-1s electrons directly encodes their relative photoionization delay. The conversion from relative streaking an-

gle $\Delta\vartheta$ to the relative photoionization delay $\Delta\tau$ is simply given by $\Delta\tau = T_L \times \Delta\vartheta/2\pi$, where T_L is the period of the streaking laser (25–31).

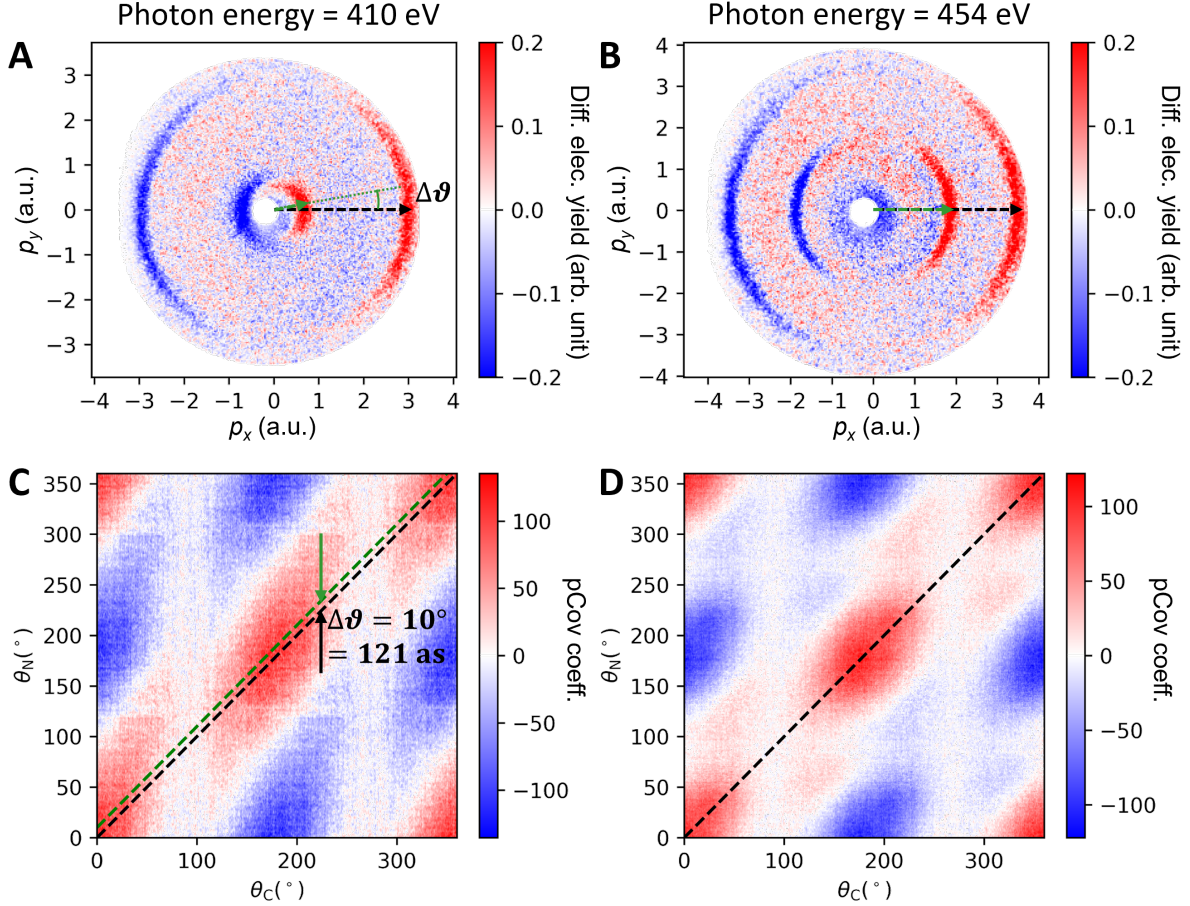


Figure 2: Using the partial covariance analysis to access the differential streaking angles. (A,B) Difference images obtained as outlined in Fig. 1, illustrating a rather large delay (at 410 eV) and a negligible delay (at 454 eV). The inner (outer) line corresponds to N-1s (C-1s) photoelectrons from pyrimidine. (C,D) Partial covariance coefficient maps between streaking-induced signal fluctuations in N-1s and C-1s photoelectrons. Given a photoionization delay $\Delta\tau = T_L \times \Delta\vartheta/2\pi$ where T_L is the streaking laser period, the streaking-induced signal fluctuation in C-1s photoelectrons at θ has the most positive covariance with streaking-induced signal fluctuation in N-1s photoelectrons around $\theta + \Delta\vartheta$. The diagonal shift in panel C represents a global differential angle $\Delta\vartheta$ corresponding to ~ 120 as photoionization time delay between the N-1s and C-1s electrons at 410 eV XFEL photon energy. As a comparison, no global diagonal shift is observed in panel D, indicating a negligible time delay at 454 eV XFEL photon energy.

Figure 2 illustrates how the relative streaking angles $\Delta\vartheta$ were obtained from the experimen-

tal data. Due to the large temporal jitter (~ 500 fs) between the arrival time of XFEL and IR laser pulses (32), the streaking directions of the core-shell photoelectrons were completely random from shot to shot. The information of relative photoionization time delay is therefore only encoded in the relative streaking angle of the N-1s and C-1s electrons, which is recorded on a shot-by-shot basis. Figure 2A shows the difference image between the average over all shots corresponding to a narrow range of streaking directions sorted by post-selection of the images and the average over all streaked images without any sorting and selection. An angular shift $\Delta\vartheta$ between the streaking directions of C-1s (outer) and N-1s (inner) electrons can be observed, which directly reflects the relative photoionization delays, as described above. To accurately determine the relative streaking angle, we employ a partial covariance analysis that utilizes the large shot-to-shot variation of streaking directions to directly extract $\Delta\vartheta$ without estimating and sorting the streaking directions of C-1s and N-1s electrons in every single image. For a given relative streaking angle $\Delta\vartheta$, the streaking-induced signal fluctuations in C-1s electrons at θ have the most positive covariance with those in N-1s electrons around $\theta + \Delta\vartheta$. By correctly calculating the partial covariance coefficients between streaking-induced signal changes in N-1s and C-1s electrons, the differential streaking angle $\Delta\vartheta$ manifests itself as a global shift in the partial covariance maps along the diagonal, as shown in Fig. 2C. Additional details on the partial covariance analysis are given in Section 2.2.1 of the supplementary material (SM). By comparing Figs. 3A,C to B,D, a relative photoionization delay of up to 120 as is observed at 410 eV, as opposed to a negligible delay at 454 eV. We have also developed a complementary data-analysis method (the so-called "center-of-mass" method), which is described in Section 2.2.2 of the SM. These two independent analysis methods yielded consistent photoionization delays (Fig. S14), which confirms the reliability and robustness of both methods.

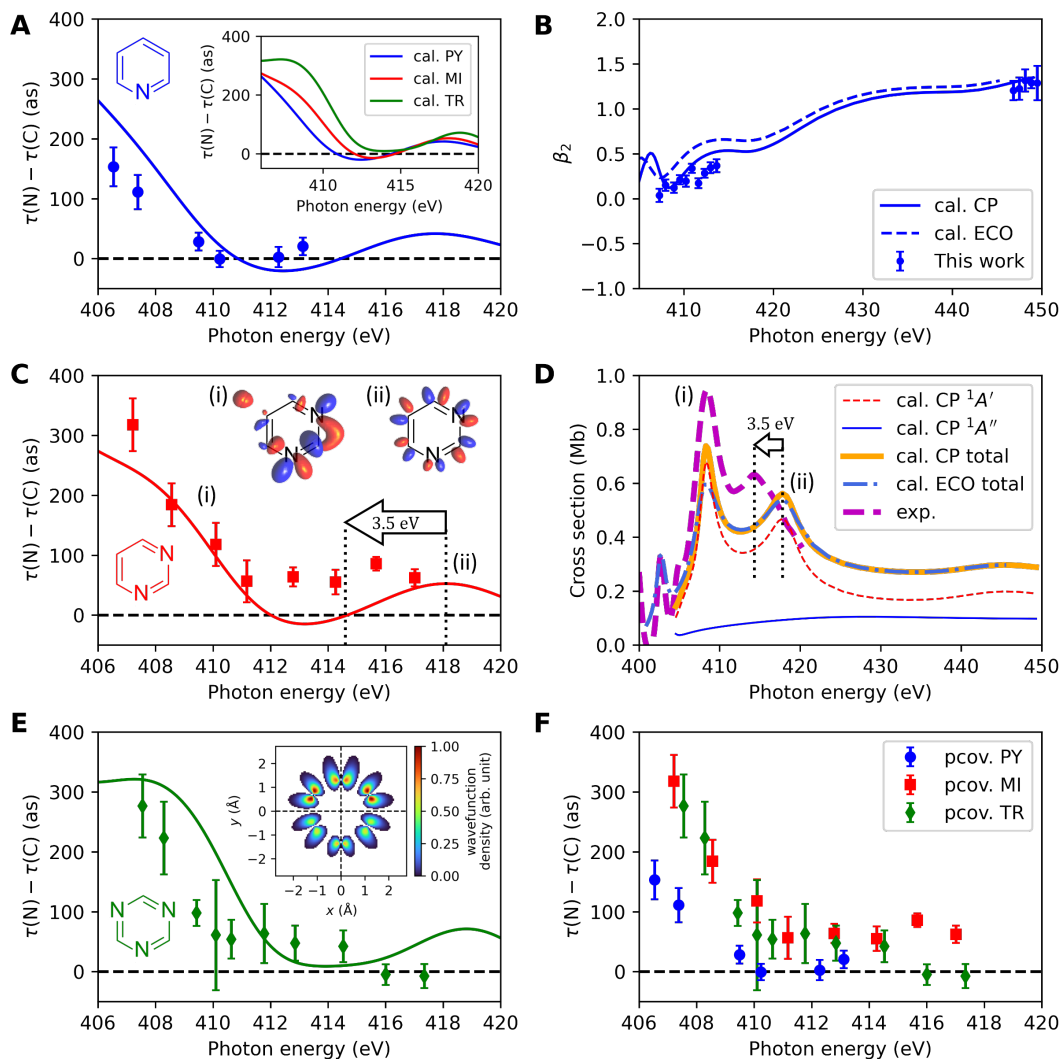


Figure 3: Energy-dependent photoionization delays and shape resonances (A, C, E) Measured relative photoionization delays ($\tau = \tau_{N1s} - \tau_{C1s}$, symbols) and calculated absolute photoionization delays including Coulomb-laser-coupling (CLC) delays (full lines) for pyridine (A), pyrimidine (C), and *s*-triazine (E), as a function of the central photon energy of the attosecond FEL pulses. Panel (F) and the inset panel in (A) compare the relative photoionization delays extracted by the partial covariance method (pcov.) and the CP calculations (cal.), respectively. The resonant one-electron wavefunctions of the two local maxima (i) and (ii) are shown as insets in (C). (B) Photoelectron asymmetry parameter of pyridine measured in the present work, compared to the CP and ECO calculations. (D) The photoionization cross sections of pyrimidine from calculation (cal.) using the ECO and CP methods and experiment (exp.). The decomposition into partial cross sections corresponding to final states of $^1A'$ and $^1A''$ symmetry of the C_s point group are also shown for the CP calculation. The arrows in (C) and (D) indicate the shift between the calculated and observed position of the higher-lying shape resonance. The inset panel of (E) illustrates the calculated wavefunction density of the *s*-triazine at photon energy of 417.7 eV, where the N atom with the core hole is located at $x = 0.00 \text{ \AA}$, $y = -1.35 \text{ \AA}$.

Figure 3 summarizes all photoionization delays measured in this work. Panels A, C, and E show the measured photoionization delays between the N-1s and C-1s photoelectrons for the three molecules, which are excellent approximations to the absolute photoionization delays of the N-1s electrons. These delays are compared to the absolute N-1s photoionization delays from core-level photoionization calculations using the Schwinger variational principle with a correlation-polarization potential, summed with the Coulomb-laser coupling (CLC) delays. Details on the calculations are given in Section 3 of the SM. The comparison of the experimental and theoretical delays among the three molecules can be found in panel F and the inset of panel A, respectively. The delays globally decrease with increasing kinetic energy, which reflects the decreasing sensitivity of faster electrons to the potential of the molecular cations. The delays of all three molecules feature local maxima between 408 and 420 eV, which are in reasonable agreement with the local maxima in the calculations. These local maxima in both experiment and theory originate from shape resonances, which correspond to a transient trapping of the photoelectron for a few tens to hundreds of attoseconds before it escapes from the molecule.

Since such shape resonances are notoriously sensitive to electron correlations and molecular structure (4, 8, 33), we have carefully benchmarked the core-level photoionization calculations against measured photoionization cross sections (Figs. 3D and S22), as well as photoelectron angular distributions measured in the present work (Figs. 3B and S23). Comparing the calculations using the equivalent-core (ECO) method with the experimental photoionization cross section (Fig. 3D) revealed very good agreement for the resonance lying below the nitrogen K-edge and the lowest-lying shape resonance after shifting the calculations to lower energies by 4.3 eV. In comparison, the correlation-polarization (CP) calculations only needed to be shifted by 0.6 eV to agree with the experimental cross sections and the calculated width of the lowest-lying shape resonance was in better agreement with the experiment than the ECO calculations. The CP calculations also agree better with the angular asymmetry parameters measured in this work (Figs. 3B and S23). Since both calculations overestimate the energetic position of the upper shape resonance by ~ 3.5 eV, we therefore identified the CP calculations as the more accurate ones and from hereon exclusively discuss these results.

Figures 3C,D demonstrate the two shape resonances of pyrimidine within the energy range, which lead to the local maxima of the cross section. The $^1A'$ symmetry component is dominating in the cross section, which displays an anti-bonding σ^* character and corresponds to the electron trapping that occurs in the molecular plane in both resonances. The insets in Fig. 3C show the one-electron representations of the corresponding resonant wavefunctions (Kapur-

Peierls states, see SM). The lower-lying shape resonance features 5 nodal planes and the upper one 6, showing that partial waves of high angular momentum are dominating the photoelectron trapping in both cases. The narrower width of the lower resonance nicely correlates with a longer photoemission delay and the broader linewidth of the upper one correlates with the shorter delay. The partial cross section corresponding to a total final-state wavefunction of $^1A''$ symmetry, i.e., anti-symmetric with respect to the molecular plane and thus a π/π^* -type continuum wavefunction, does not feature any sharp resonances, indicating that photoelectron trapping exclusively occurs in the molecular plane of pyrimidine. The probability density of the resonant wavefunction of *s*-triazine at ~ 418 eV is illustrated in the inset of Fig. 3E and in Fig. 4. Similar resonances occur in all three molecules, as shown in Fig. S20.

Since our measurements extend to within ~ 2 eV of the N-1s ionization threshold, they are particularly sensitive to the CLC delays. It has previously been shown that CLC delays in attosecond streaking experiments are equivalent to the continuum-continuum (cc) delays known from RABBIT measurements (3). The most commonly used approximation, known as “P”, only includes the phase of the continuum-continuum (cc) matrix elements (34). The “P+A” formula additionally contains a long-range amplitude correction. Through detailed comparisons of these (and two more) formulae with calculations based on the time-dependent Schrödinger equation (TDSE, see Fig. S24A), we found that the arithmetic average of “P” and “P+A” agreed best with the TDSE. We therefore used those results in Figs. 3 and 4 of the present article and show the other results in the remainder of Fig. S24. We also investigated the role of the Auger decay and the post-collision interaction (PCI) between the Auger electron and the photoelectron. We find that the correction of the Coulomb delay from a singly- to a doubly-charged cation is nearly compensated by the delay that is caused by the PCI effect (Fig. S25). Since these corrections are small and do not affect the relative delays between the molecular species that we studied, we refer the interested reader to the SM, and neglect these corrections for the remainder of the present discussion.

These results open the novel opportunity to analyze the mechanisms that govern the trapping of the photoelectron on the attosecond time scale. Figure 4 illustrates the trapping of the outgoing photoelectron wave in the higher-lying (418 eV) resonance of *s*-triazine. The atomic cores provide attractive potentials in their vicinities, while the centrifugal energy creates a repulsive region at the center of the aromatic ring. Their addition results in a potential barrier (black curve in Fig. 4) which traps the resonant wavefunction for a duration of ~ 360 as. The photoelectron wave initially originates from the 1s shells of the nitrogen atoms and then scatters in

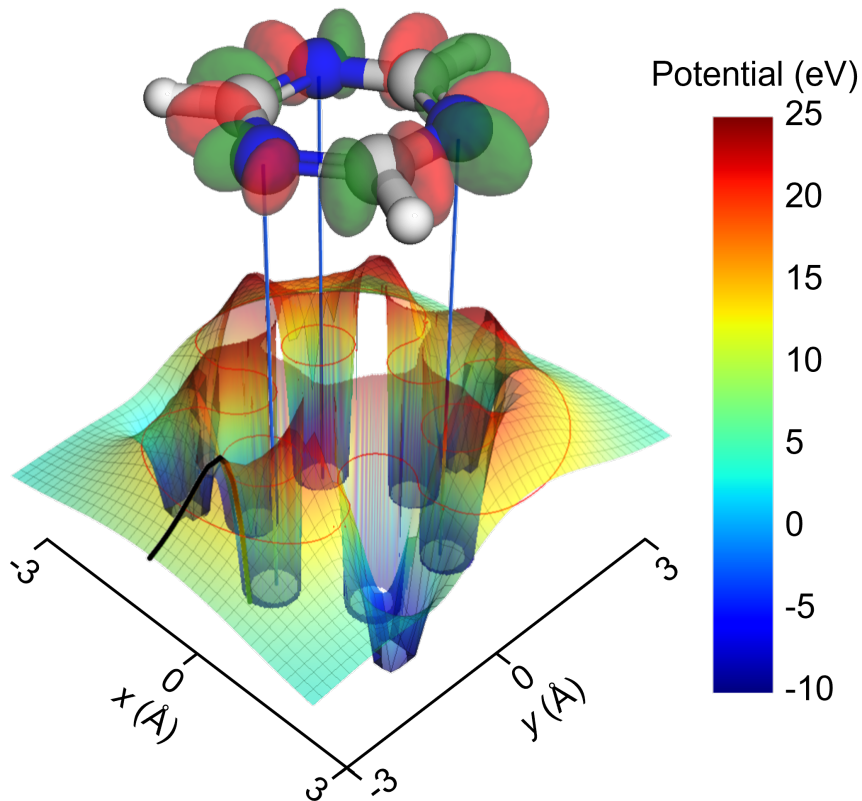


Figure 4: **Illustration of the mechanism of electron trapping in *s*-triazine.** The electrostatic potential of the *s*-triazine cation summed with the centrifugal potential corresponding to $L = 6$ is plotted as the false-colored surface. The red line shows the contour at 12.8 eV, the energy of the resonance illustrated on top of the figure ((apur-Peierls state with isosurfaces of +0.1 (red) and -0.1 (green)). The vertical blue lines map the N atoms to their coordinates on the xy -plane. The black curve illustrates the tunneling barrier that traps the resonant wave function.

the molecular potential, which results in comparable amplitudes of the resonant wave function on all atoms of the molecular ring. But what causes the increase of the photoionization delays and resonance lifetimes with increasing number of nitrogen atoms and increasing symmetry?

To answer this question, Figure 5A shows a sketch of effective radial potentials which indicate the height of the angular-momentum barrier for different values of the angular momentum, L , and Figs. 5C,E,G show the absolute squares of resonant one-electron wavefunctions, resolved into partial waves of angular momentum L and irreducible representations of the respective point groups (specified in each panel). Figure 5B shows the CLC delays and Figs. 5D,F,H show the calculated delays for all three molecules. Because of its isolated nature and visibility

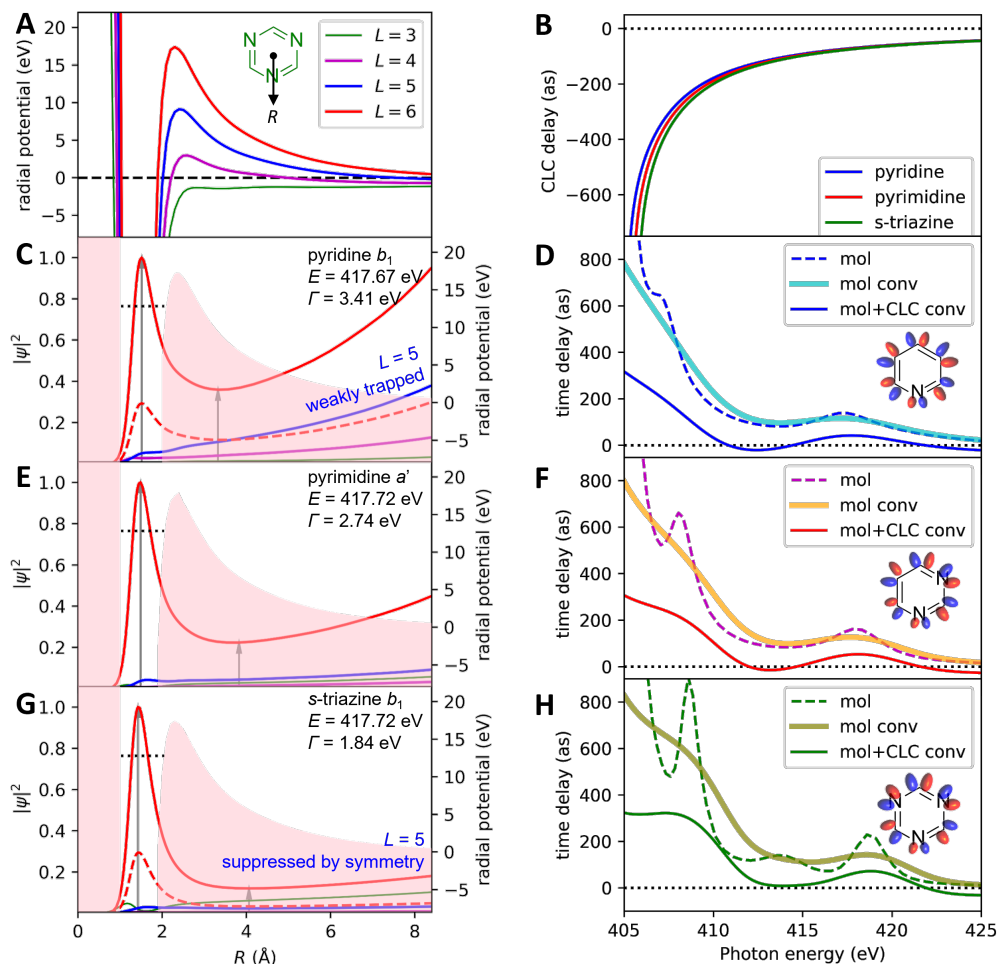


Figure 5: **Mechanisms of photoelectron trapping in the azabenzene molecules** (A) Sketch of radial potentials of s -triazine along a line connecting the center of the aromatic ring to the ionized N atom (indicated as the inset) with the angular-momentum barriers of different L . (B) CLC delays for the three molecules. (C,E,G) Resonant wavefunctions (Kapur-Peierls states) corresponding to the shape resonance centered at the energies indicated in the insets, decomposed into partial waves indicated by the same color code in (A). Only the most contributing components are plotted, and more than one component may belong to the same L (the second component is plotted in dashed line). The shaded areas correspond to the radial potentials of the corresponding molecules with the angular-momentum barrier of $L = 6$ along the direction defined in (A). (D,F,H) Molecular photoionization delays as obtained from the CP calculations (dashed lines), total delays obtained by adding the CLC delays to the molecular delays (thin full lines) and convolution of the total delays with a 3.8-eV FWHM Gaussian line profile (thick full lines). The resonant wavefunction at 417 ~ 420 eV for each molecule is illustrated as the inset in the corresponding panel.

in the experimental results (Fig. 3C), we focus the remainder of this discussion on the shape resonance located at 417-420 eV in each molecule.

In all three molecules, the partial wave(s) with $L = 6$ dominate(s) in amplitude, which is the consequence of the high barrier in the radial potential (panel A) arising from the centrifugal-potential contribution $\hbar^2 L(L + 1)/(2m_e R^2)$, where m_e is the mass of the electron and R its distance from the center of charge. The effective potentials of $L = 6$ are indicated by the shaded areas in the corresponding panels. It is clear that the main part of the wavefunction is confined in the quasi-bound region in the vicinity of the N and C atoms, while a tail tunnels through the barrier. In the case of pyridine (Fig. 5A), the dominant $L = 6$ partial wave is least-well trapped compared to the other molecules, which manifests itself in the ratio of the absolute-square amplitudes of the resonant wavefunction between the local maximum at small R and the local minimum indicated by the second grey arrow in Figs. 5C,E,G. This identifies tunneling through an angular-momentum barrier as the first mechanism governing electron trapping in the azabenzene series and shows that the trapping strength of the dominant partial wave increases in the order pyridine, pyrimidine, *s*-triazine. This shows that substituting a C-H group with the more electronegative N atom increases the trapping strength and therefore the lifetime of the resonance. We note that the divergence of the Kapur-Peierls state for large R is a consequence of their mathematical nature, specifically their complex-valued momentum, see SM Section 3.2.

Figure 5 also reveals a second mechanism at play. In addition to the changing amplitude ratio between the wavefunctions in the quasi-bound and tunneling regions, we also observe the manifestation of molecular symmetry. Whereas pyridine displays sizable contributions from an $L = 5$ partial wave, which can be identified as being weakly trapped from the very low amplitude of its quasi-bound part, the contributions of $L = 5$ are much weaker in pyrimidine and barely visible in *s*-triazine as a consequence of symmetry. The three-fold (D_{3h}) symmetry of the *s*-triazine scaffold is indeed the reason why $L = 6$ and $L = 3$ partial waves are dominant and other partial waves are suppressed in that case. The suppression of these lower- L , more weakly trapped partial waves, to which the $L = 6$ partial waves can couple to release the photoelectron more efficiently, explains the increasing lifetime of the shape resonance in the series pyridine, pyrimidine, *s*-triazine.

To summarize, these two mechanisms explain the trend in the resonant photoelectron trapping times in the azabenzene series. This trend is most clearly visualized in Figs. 5D,F,H, which show that the photoionization delays in the vicinity of the discussed shape resonance indeed increase in the sequence pyridine, pyrimidine, *s*-triazine.

In conclusion, we have used the novel attosecond capabilities of LCLS to measure core-level photoionization delays of aromatic molecules. These measurements were made possible by the combination of attosecond X-ray pulses with the angular streaking technique. Absolute N-1s photoionization delays were accessed by using the much faster C-1s photoelectrons as a time reference. These self-referenced measurements were realized on a fine energy grid and revealed the presence of local maxima at 3-15 eV above the N-1s threshold. Comparison to advanced core-level photoionization calculations identified two dominant shape resonances in each molecule and showed that photoelectron trapping occurs in the plane of the aromatic molecules. The two dominant mechanisms governing the photoelectron trapping were identified as (i) changes in the barrier height of the molecular potential that lead to an increase of the electron trapping with increasing electronegativity of the functional groups and (ii) the increasing symmetry of the molecular scaffold reduces the coupling between the well-trapped high- L and the less-trapped lower- L states. Both effects individually and collectively increase the trapping time in the sequence pyridine, pyrimidine, *s*-triazine. These results demonstrate the promise of performing attosecond core-level photoemission experiments at free-electron-laser facilities for the following reasons. The studied molecules are indeed key building blocks of biologically active molecules, as well as molecules employed in optoelectronics, which opens the perspective of studying attosecond electron dynamics in these systems. The key advantage of core-level photoionization delays over valence-shell photoionization delays, is that the photoelectron spectra always remain simple, featuring only one dominant peak per atom of a given type. This will enable the application of the methods described in this work to complex molecules, molecular assemblies and polymers, such as organic semiconductors. Specifically, the effects governing the attosecond electron trapping in aromatic systems unveiled in the present work may become guiding principles for the design and interpretation of experiments studying charge migration and charge transfer in functional materials.

Acknowledgments

Funding: Use of the Linac Coherent Light Source (LCLS), SLAC National Accelerator Laboratory, is supported by the U.S. Department of Energy, Office of Science, Office of Basic Energy Sciences under Contract No. DE-AC02-76SF00515. The work of J.-B.J., X.G., D.H., M.H., S.H. and H.J.W. was supported by ETH Zürich and project 200021_172946 of the Swiss National Science Foundation. The work of M.H. was additionally supported by the European

Union's Horizon 2020 research and innovation program under the Marie Skłodowska-Curie grant agreement No 801459 - FP-RESOMUS. The effort from T.D.D., J.T.O. A.L.W., J.W., T.J.A.W and J.P.C. was supported by DOE, BES, Chemical Sciences, Geosciences, and Biosciences Division (CSGB). Z.G, D.C., J.D., P.L.F., R.R. and A.M. acknowledge support from the Accelerator and Detector Research Program of the Department of Energy, Basic Energy Sciences division. Z.G., P.L.F. and R.R. also acknowledge support from Robert Siemann Fellowship of Stanford University. The effort by R.R.L. and C.W.M. at LBNL was supported by the U.S. DOE BES, CSGB under Contract No. DE-AC02-05CH11231. Calculations at LBNL made use of the resources of the National Energy Research Scientific Computing Center, a DOE Office of Science User Facility, and the Lawrence computational cluster resource provided by the IT Division at the LBNL. C.S.T. was supported in part by the Berkeley Lab Undergraduate Faculty Fellowship (BLUFF) Program, managed by Workforce Development & Education at Berkeley Lab.

Author Contributions: J.-B.J., T.D., K.U., A.M., J.P.C. and H.J.W. conceived the experiment. All authors contributed to the realization of the experiment and discussed the results. J.-B.J., Z.G. and T.D. developed the data-analysis methodology. J.-B.J. and Z.G. analyzed the data. R.R.L., C.S.T. and C.W.M. performed the calculations of molecular photoionization delays. J.-B.J., Z.G. and H.J.W. wrote the initial draft of the manuscript, which was reviewed and edited by all authors. **Competing Interests:** The authors declare no competing interests. **Data availability statement:** All data will be made available on the public ETH data repository upon acceptance of the manuscript.

References and Notes

1. M. Schultze, *et al.*, *Science* **328**, 1658 (2010).
2. K. Klünder, *et al.*, *Phys. Rev. Lett.* **106**, 143002 (2011).
3. R. Pazourek, S. Nagele, J. Burgdörfer, *Rev. Mod. Phys.* **87**, 765 (2015).
4. M. Huppert, I. Jordan, D. Baykusheva, A. von Conta, H. J. Wörner, *Phys. Rev. Lett.* **117** (2016).
5. J. Vos, *et al.*, *Science* **360**, 1326 (2018).
6. S. Biswas, *et al.*, *Nat. Phys.* **16**, 778 (2020).

7. A. Kamalov, A. L. Wang, P. H. Bucksbaum, D. J. Haxton, J. P. Cryan, *Physical Review A* **102**, 023118 (2020).
8. S. Nandi, *et al.*, *Science Advances* **6**, eaba7762 (2020).
9. S. Heck, *et al.*, *Science advances* **7**, eabj8121 (2021).
10. X. Gong, *et al.*, *Nature* **609**, 507 (2022).
11. S. Heck, *et al.*, *Physical review letters* **129**, 133002 (2022).
12. I. Jordan, *et al.*, *Science* **369**, 974 (2020).
13. A. L. Cavalieri, *et al.*, *Nature* **449**, 1029 (2007).
14. S. Neppl, *et al.*, *Nature* **517**, 342 (2015).
15. Z. Tao, *et al.*, *Science* **353**, 62 (2016).
16. F. Siek, *et al.*, *Science* **357**, 1274 (2017).
17. J. Duris, *et al.*, *Nature Photonics* **14**, 30 (2020).
18. S. Li, *et al.*, *Optics express* **26**, 4531 (2018).
19. S. Li, *et al.*, *Science* **375**, 285 (2022).
20. Y. Ling, *et al.*, *Drug Design, Development and Therapy* pp. 4289–4338 (2021).
21. T. P. Selvam, C. R. James, P. V. Dniandev, S. K. Valzita, *Research in Pharmacy* **2** (2015).
22. A. Sharma, R. Sheyi, B. G. de la Torre, A. El-Faham, F. Albericio, *Molecules* **26**, 864 (2021).
23. A. Moliton, *Optoelectronics of molecules and polymers*, vol. 104 (Springer, 2010).
24. P. Walter, *et al.*, *Journal of Synchrotron Radiation* **29**, 957 (2022).
25. Z. Zhao, Z. Chang, X. Tong, C. Lin, *Optics express* **13**, 1966 (2005).
26. P. Eckle, *et al.*, *Nature Physics* **4**, 565 (2008).

27. A. Kazansky, A. Bozhevolnov, I. Sazhina, N. Kabachnik, *Physical Review A* **93**, 013407 (2016).
28. A. Kazansky, I. Sazhina, N. Kabachnik, *Optics Express* **27**, 12939 (2019).
29. N. Hartmann, *et al.*, *Nature Photonics* **12**, 215 (2018).
30. A. S. Kheifets, *et al.*, *Physical Review A* **106**, 033106 (2022). Publisher: American Physical Society.
31. V. V. Serov, A. S. Kheifets, *Journal of Physics B: Atomic, Molecular and Optical Physics* **56**, 025601 (2023).
32. J. M. Glowina, *et al.*, *Optics express* **18**, 17620 (2010).
33. M. Piancastelli, *Journal of Electron Spectroscopy and Related Phenomena* **100**, 167 (1999).
34. J. M. Dahlström, A. L'Huillier, A. Maquet, *Journal of Physics B: Atomic, Molecular and Optical Physics* **45**, 183001 (2012).
35. Z. Zhang, *et al.*, *New Journal of Physics* **22**, 083030 (2020).
36. M. Seaberg, *et al.*, *Synchrotron Radiation News* **35**, 20 (2022). Publisher: Taylor & Francis
_eprint: <https://doi.org/10.1080/08940886.2022.2066416>.
37. S. Li, *et al.*, *AIP Advances* **8**, 115308 (2018). Publisher: American Institute of Physics.
38. R. Obaid, *et al.*, *Journal of Physics B: Atomic, Molecular and Optical Physics* **51**, 034003 (2018). Publisher: IOP Publishing.
39. M. C. Hettrick, J. H. Underwood, P. J. Batson, M. J. Eckart, *Applied optics* **27**, 200 (1988).
40. A. E. Orel, T. N. Rescigno, B. H. Lengsfeld Iii, *Physical Review A* **42**, 5292 (1990). PRA.
41. F. A. Gianturco, R. R. Lucchese, N. Sanna, *Journal of Chemical Physics* **100**, 6464 (1994).
42. A. P. P. Natalense, R. R. Lucchese, *Journal of Chemical Physics* **111**, 5344 (1999).
43. J. P. Perdew, A. Zunger, *Physical Review B* **23**, 5048 (1981).
44. J. Dunning, Thom H., *Journal of Chemical Physics* **90**, 1007 (1989).

45. C. A. Marante, *et al.*, *Physical Review A* **102**, 012815 (2020). PRA.
46. M. Hoshino, *et al.*, *Journal of Physics B: Atomic, Molecular and Optical Physics* **51**, 065402 (2018).
47. G. Vall-Ilosera, *et al.*, *Journal of Chemical Physics* **128** (2008).
48. R. R. Lucchese, F. A. Gianturco, *International Reviews in Physical Chemistry* **15**, 429 (1996).
49. A. M. Lane, D. Robson, *Physical Review* **151**, 774 (1966). PR.
50. H. D. Meyer, O. Walter, *Journal of Physics B: Atomic and Molecular Physics* **15**, 3647 (1982).
51. V. I. Kukulin, V. M. Krasnopol'sky, J. Horáček, *Theory of Resonances: Principles and Applications* (Springer Netherlands, Dordrecht, 1989).
52. J. M. Dahlström, *et al.*, *Chemical Physics* **414**, 53 (2013).
53. V. V. Serov, V. L. Derbov, T. A. Sergeeva, *Advanced Lasers: Laser Physics and Technology for Applied and Fundamental Science*, O. Shulika, I. Sukhoivanov, eds., Springer Series in Optical Sciences (Springer Netherlands, Dordrecht, 2015), pp. 213–230.
54. C. Nicolas, C. Miron, *Journal of Electron Spectroscopy and Related Phenomena* **185**, 267 (2012).

Supplementary Material for Attosecond Core-level Photoionization Delays of Aromatic Molecules

Jia-Bao Ji,^{1*} Zhaoheng Guo,^{2,3,4*} Taran Driver,^{2,3} Cynthia S. Trevisan,⁵,
David Cesar,² Xinxin Cheng,² Joseph Duris,² Paris L. Franz,^{2,3} James Glowonia,²
Xiaochun Gong,^{1,6} Daniel Hammerland,¹ Meng Han,^{1,7} Saijoscha Heck,¹
Matthias Hoffmann,² Andrei Kamalov,² Kirk A. Larsen,^{2,3} Xiang Li,²
Ming-Fu Lin,² Yuchen Liu,^{8,9} C. William McCurdy,^{8,9} Razib Obaid,²
Jordan T. O'Neal,³ Thomas N. Rescigno,⁸ River R. Robles,^{2,3} Nicholas Sudar,^{2,3}
Peter Walter,² Anna L. Wang,^{2,3} Jun Wang,^{2,3} Thomas J. A. Wolf,^{2,3} Zhen Zhang,²
Kiyoshi Ueda,^{1,10,11} Robert R. Lucchese,^{8†} Agostino Marinelli,^{2,3†}
James P. Cryan,^{2,3†} Hans Jakob Wörner^{1†}

¹Laboratory of Physical Chemistry, ETH Zürich, Zurich, Switzerland

²SLAC National Accelerator Laboratory, Menlo Park, CA, USA

³Stanford PULSE Institute, SLAC National Accelerator Laboratory, Menlo Park, CA, USA

⁴Laboratory for Ultrafast X-ray Sciences, EPFL, Lausanne, Switzerland

⁵California State University, Maritime Academy, Vallejo, CA, USA

⁶State Key Laboratory of Extreme Photonics and Instrumentation,

College of Optical Science and Engineering, Zhejiang University, Hangzhou 310058, China

⁷J. R. Macdonald Laboratory, Department of Physics, Kansas State University, Manhattan, KS, USA

⁸Lawrence Berkeley National Laboratory, Berkeley, CA, USA

⁹Department of Chemistry, University of California, Davis, CA, USA

¹⁰Department of Chemistry, Tohoku University, Sendai, Japan

¹¹School of Physical Science and Technology, ShanghaiTech University, Shanghai, China

*These authors contributed equally.

†To whom correspondence should be addressed;

E-mail: rlucchese@lbl.gov, marinelli@slac.stanford.edu, jcryan@stanford.edu,
hwoerner@ethz.ch.

Contents

1	Experimental Methodology	3
1.1	Attosecond soft X-ray pulses from LCLS	3
1.2	Attosecond angular streaking	4
2	Data analysis	5
2.1	Image Preprocessing	5
2.2	Determination of Photoionization Delays	5
2.2.1	Partial Covariance Analysis	5
2.2.2	Center-of-mass analysis	10
2.2.3	Comparison of the two methods	18
2.3	Determination of Photoelectron Asymmetry Parameters	18
3	Theoretical Methodology	21
3.1	Core-level photoionization calculations	21
3.2	Characterization of the resonances above the N K-edge of the azabenzenes.	21
4	Additional comparisons between experiment and theory	27
4.1	Comparison of experimental and theoretical cross sections and asymmetry parameters . .	27
4.2	Comparison of Coulomb-laser coupling delays with TDSE and experiments	29
4.3	The role of post-collision interactions	31

1 Experimental Methodology

1.1 Attosecond soft X-ray pulses from LCLS

To generate attosecond pulses with an X-ray free-electron laser (XFEL), we create a high current spike in the relativistic electron bunch using temporal shaping of the photocathode laser pulse (35). This electron bunch produces an isolated attosecond SXR pulse after passing through the undulator line of the Linac Coherent Light Source (LCLS). To shape the temporal profile of the photocathode laser, we used an interferometer to create a pulse shape with a temporal notch at the center of the pulse. Such a laser profile produces an electron bunch with a modulated current profile, i.e. there is a local minimum of current profile in the electron bunch core. This current modulation was amplified to produce a high current spike in the downstream accelerator via the microbunching instability. The electron bunch was accelerated to 5 GeV before entering the undulator, and has a peak current of ~ 10 kA and ~ 1.5 fs full width at half maximum (FWHM) duration. The positive energy chirp of the electron beam was on the order of 1% of the electron bunch central energy. The undulator beam line is tapered to match this energy chirp, which results in a gigawatt-level single isolated attosecond pulse (17). Such a large undulator taper ($\sim 0.15\%$ per module) was much larger than the acceptance of the XFEL, which therefore suppressed the background XFEL radiation outside of the main current spike. Figure S1 shows the distributions of XFEL pulse energies and FWHM bandwidths in a dataset with 416 eV central X-ray photon energy. The mean pulse energy is 39 μ J and the mean FWHM bandwidth is 3.8 eV. From our previous measurements, we can estimate a FWHM temporal pulse duration of 460 as for the X-ray pulses.

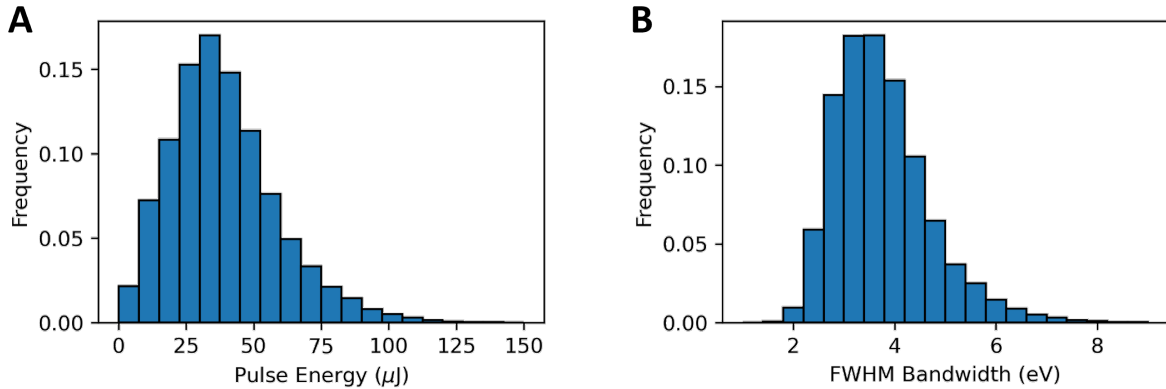


Figure S1: Distributions of pulse energies (A) and FWHM bandwidths (B) of single isolated soft X-ray XFEL pulses. We limit our analysis of FWHM bandwidth to shots with top 50% of pulse energies to increase the signal-to-noise ratio.

The XFEL central photon energy could be continuously adjusted by tuning the undulator gap to adjust the undulator parameter, K . We scanned the XFEL central photon energy from just below the nitrogen K -edge up to 418 eV to study the energy-dependent photoionization delays between nitrogen and carbon K -shell photoemission features. We jumped to ~ 450 eV to take a reference measurement, where both photoelectrons have a high kinetic energy, and we expect a negligible photoemission delay.

Electrode Number	Voltage (V)
1	-1073
2	-1522
3	-1973
4 (Repeller)	-1973
5 (Extractor)	-1403
6	-1300
7	-1243
8	-1100
9	-950
10	-803
11	-657
12	-510
13	-364
14	-290
MCP Front	0

Table S1: Voltage settings for co-axial velocity map imaging (c-VMI) (37) spectrometer used to collect x-ray ionized photoelectrons.

1.2 Attosecond angular streaking

Our measurements were performed at the TMO end station of the Linac Coherence Light Source (LCLS). The attosecond x-ray pulses described above were focused to a spot-size of $\sim 30 \mu\text{m}$ in diameter using a pair of Kirkpatrick-Baez focusing mirrors (36). The x-ray beam was focused into the co-axial velocity map imaging (c-VMI) spectrometer (37) which collected photoelectrons ionized from the target molecules. At the interaction point of the c-VMI, the x-ray beam was overlapped with a focused 1300 nm, circularly polarized “streaking” field.

The 1300-nm streaking pulse with a duration of ~ 40 fs was produced by a commercial optical parametric amplifier (TOPAS-HE, Light Conversion) which is pumped by a ~ 30 fs, 9 mJ, 800-nm laser source. The signal and idler beams were separated by a dichroic mirror and the signal beam was sent through a superachromatic quarter-wave plate (Thorlabs SAQWP05M-1700) to produce a circularly polarized laser field. The 1300-nm signal beam was then focused with a $f = 600$ mm CaF_2 lens before being reflected from a silver-coated mirror with a 2-mm-diameter hole to co-propagate the laser and x-ray fields to the interaction point. The focus of the IR laser is shifted 1 – 2 mm downstream of the interaction point to mitigate the effects of the Gouy phase of the IR-field across the focal volume.

The sample molecules were introduced via a skimmed, molecular beam source. High pressure (6.4 bar) helium gas is bubbled through a vessel heated to 80-140°C containing one of the sample molecules. The sample is injected into the vacuum chamber by a pulsed valve, which is separated from the main chamber by a 2 mm diameter skimmer.

The electrostatic lens of the c-VMI spectrometer was set for an optimal resolution on the high-energy electrons photoionized from the carbon K -shell following the procedure outlined in Ref. (37). The experimental voltages are outlined in Table S1.

Downstream of the interaction point, the TMO beamline features an x-ray photon spectrometer featuring a variable-line spaced (VLS) grating (38, 39). This spectrometer measures the incident x-ray spectrum for each x-ray shot. This information is used to sort the data as described below.

2 Data analysis

2.1 Image Preprocessing

To account for errors in the imaging system we process the raw image data. We apply a transformation to the raw image from the c-VMI detector so that both the nitrogen K -shell and carbon K -shell photoemission features have the expected circular momentum distribution in the absence of the streaking laser field. The momentum distribution is then further processed to extract the photoemission delay (Sec. 2.2) and the photoelectron asymmetry parameters (Sec. 2.3).

2.2 Determination of Photoionization Delays

The relative photoionization delay between the carbon and nitrogen K -shell photoemission features, $\Delta\tau$, is related to the difference in streaking angle, $\Delta\vartheta$, between the momentum shift of the nitrogen and carbon photoemission features,

$$\Delta\tau = T_L \times \Delta\vartheta/2\pi, \quad (\text{S1})$$

where $T_L = 4.33$ fs is the period of the IR streaking laser.

We use two methods to extract the differential streaking angle $\Delta\vartheta$ from the dataset. The first method (Sec. 2.2.1), uses a partial covariance approach to isolate the correlated changes of streaking-induced variations in the photoelectron momentum distribution. A second procedure (Sec. 2.2.2), uses a sorting method which tags the arrival time of the attosecond x-ray pulse relative to the IR-field. Following the sorting, a fast Fourier Transform across this sorting direction is then applied to the momentum distribution. A global phase shift $\Delta\vartheta$ between the nitrogen and carbon K -shell photoelectrons is extracted from the transformed data, as further described below.

2.2.1 Partial Covariance Analysis

In the partial covariance analysis, we directly determine $\Delta\vartheta$ by studying the correlated changes of streaking-induced signal variations in two photoemission features, circumventing the need of sorting the XFEL arrival time on a single-shot basis. Given a relative photoionization delay $\Delta\tau = T_L \times \Delta\vartheta/2\pi$, the streaking-induced signal change in the C-1s photoline at detector angle θ has the best joint variability with the streaking-induced signal change in the N-1s photoline at detector angle $\theta + \Delta\vartheta$. Therefore, the information of $\Delta\vartheta$ is encoded in the covariance between streaking-induced signal changes in two photoemission features. Here the covariance between two variables A and B is defined as:

$$\text{Cov}[A, B] = \langle AB \rangle - \langle A \rangle \langle B \rangle, \quad (\text{S2})$$

where $\langle \cdot \rangle$ denotes the statistical average.

The mathematical model behind the covariance analysis is detailed in another publication under preparation. Here we give a brief introduction to the data analysis pipeline for this publication. Given a

dataset of c-VMI data, we calculate two 1-D traces, namely $X(\theta_C)$ for C-1s photoelectrons and $Y(\theta_N)$ for N-1s photoelectrons, on every single-shot streaked c-VMI image. The Region of Interest (ROI) for integrating each 1-D trace is taken on the high-energy flank of the corresponding unstreaked photoemission feature. Essentially, the lower bound of the ROI is strictly determined by the maximal gradient of the radial electron yield in the average unstreaked c-VMI image, as shown in Fig. S2. The selection of the upper bound of the ROI is not strict. In our data analysis, we chose the upper bound of the ROI to be high enough to cover a sufficient range of the streaked signal, without including too much of the X-ray artifacts. The latter originate from X-ray radiation that is diffracted on slits along the beam path and scattered onto the MCP detector. Since these artifacts change with the X-ray-photon energy, they can result in unwanted joint variability in the covariance analysis. Two 1-D traces $X(\theta_C)$ and $Y(\theta_N)$ contain the information of streaking-induced signal changes in the C-1s and N-1s photoemission features.

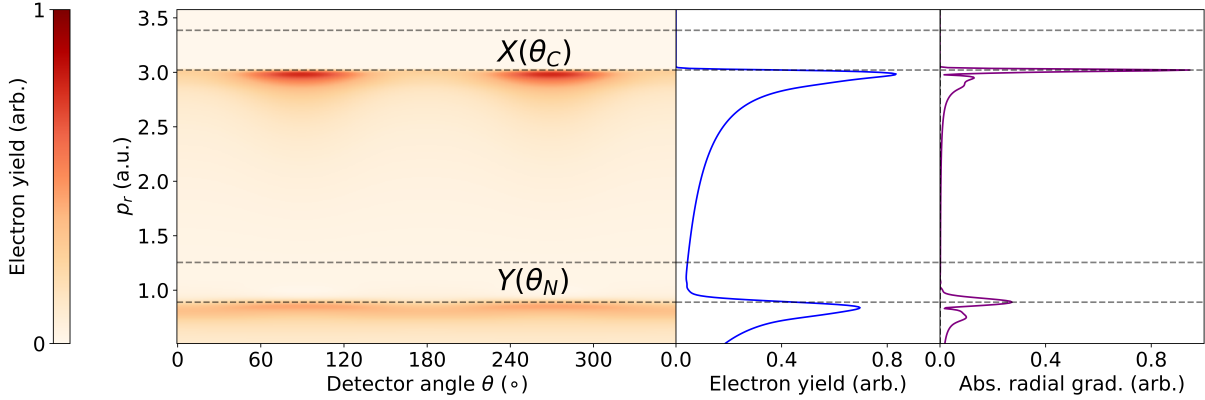


Figure S2: Regions of Interest (ROIs) used in the partial covariance analysis of photoionization delays. The false-color map in the left panel shows the polar-rebinned average unstreaked c-VMI image of pyrimidine data, ionized by 417 eV XFEL pulses. The blue curve in the middle panel shows the radial electron yield integrated over all detector angles. The purple curve in the right panel shows the absolute value of the radial gradient of data shown in the middle panel. Two pairs of dashed lines present lower and upper bounds of collecting signal in C-1s ($X(\theta_C)$) and N-1s ($Y(\theta_N)$) photoelectrons for the partial covariance analysis of photoionization delays.

We aim to study the covariance between streaking-induced signal changes in C-1s and N-1s photoemission features. However, besides streaking-induced momentum shifts, fluctuations in XFEL pulse properties can also induce correlated signal changes, notably in the high-energy flanks of two photoemission features. For example, the electron yield in both photoemission features changes together with the XFEL pulse energy. To this end, we employ the rotation symmetry of the unstreaked c-VMI image and utilize the fact that the streaking-induced momentum shift breaks the rotational symmetry. We define the anti-symmetric traces of $X(\theta_C)$ and $Y(\theta_N)$ as:

$$\begin{aligned}\tilde{X}(\theta_C) &= \frac{1}{2} (X(\theta_C) - X(\theta_C + \pi)), \\ \tilde{Y}(\theta_N) &= \frac{1}{2} (Y(\theta_N) - Y(\theta_N + \pi)).\end{aligned}\tag{S3}$$

The covariance $\text{Cov}[\tilde{X}(\theta_C), \tilde{Y}(\theta_N)]$ mainly describes the joint variability between streaking-induced signal changes in two photoemission feature. In our data analysis, we notice that there are some X-ray artifacts near the central hole of the c-VMI. These X-ray artifacts do not shift with the streaking laser. However, they are X-ray pulse-energy dependent and they are also not symmetric in geometry. The anti-symmetrization defined in Eqs. S3 can not get rid of these X-ray artifacts. To better remove the effect of these X-ray artifacts on our covariance analysis, we further use the following partial covariance to study the photoionization delay,

$$\text{pCov}[\tilde{X}(\theta_C), \tilde{Y}(\theta_N); I(\omega)] = \text{Cov}[\tilde{X}(\theta_C), \tilde{Y}(\theta_N)] - \text{Cov}[\tilde{X}(\theta_C), I(\omega)] \text{Cov}^{-1}[I(\omega), I(\omega)] \text{Cov}[I(\omega), \tilde{Y}(\theta_N)], \quad (\text{S4})$$

where $I(\omega)$ is the single-shot X-ray spectrum measured on VLS. The sum of $I(\omega)$ is a measurement of the single-shot XFEL pulse energy. The partial covariance coefficient defined in Eq. S4 resolves the linear dependence of the X-ray artifacts on the X-ray pulse energy. As a result, the partial covariance coefficient defined in Eq. S4 gets rid of most contributions from the X-ray artifacts, and is dominated by the information on the joint variability in streaking-induced signal changes. We use the 2-D partial covariance map $\text{pCov}[\tilde{X}(\theta_C), \tilde{Y}(\theta_N); I(\omega)]$ as a function of (θ_C, θ_N) to analyze photoionization delays.

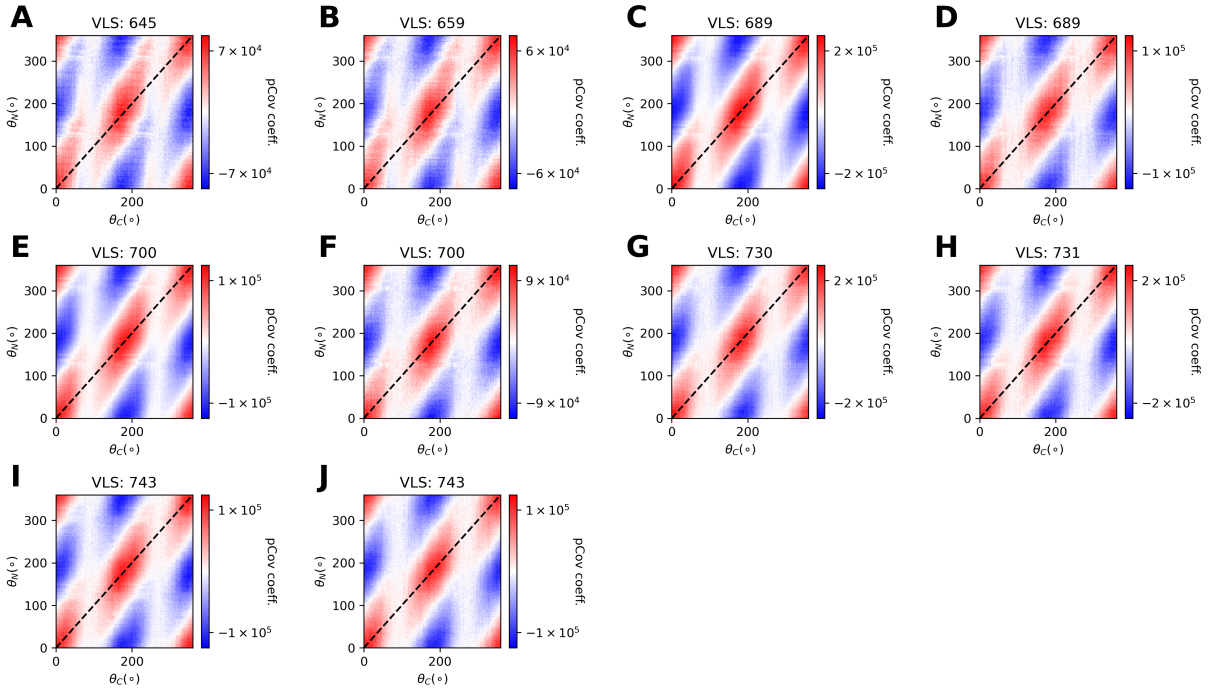


Figure S3: Partial covariance maps calculated on pyridine data. The false-color map in each panel shows the partial covariance map calculated on streaked c-VMI data with VLS centroids in a certain bin. The title of each panel shows the mean value of VLS centroids of data in this bin. Data in panels **A, B, C, E, H, I** were taken with the MCP voltages listed in Table S1. Data in panels **D, F, G, J** were taken with 1.1 times the MCP voltages listed in Table S1.

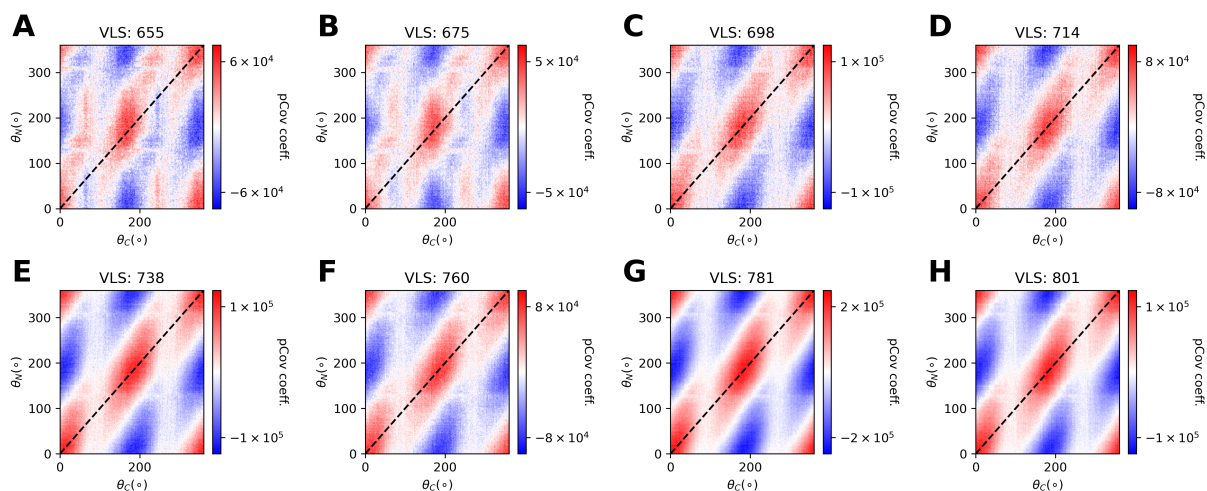


Figure S4: Partial covariance maps calculated on pyrimidine data. The false-color map in each panel shows the partial covariance map calculated on streaked *c*-VMI data with VLS centroids in a certain bin. The title of each panel shows the mean value of VLS centroids of data in this bin.

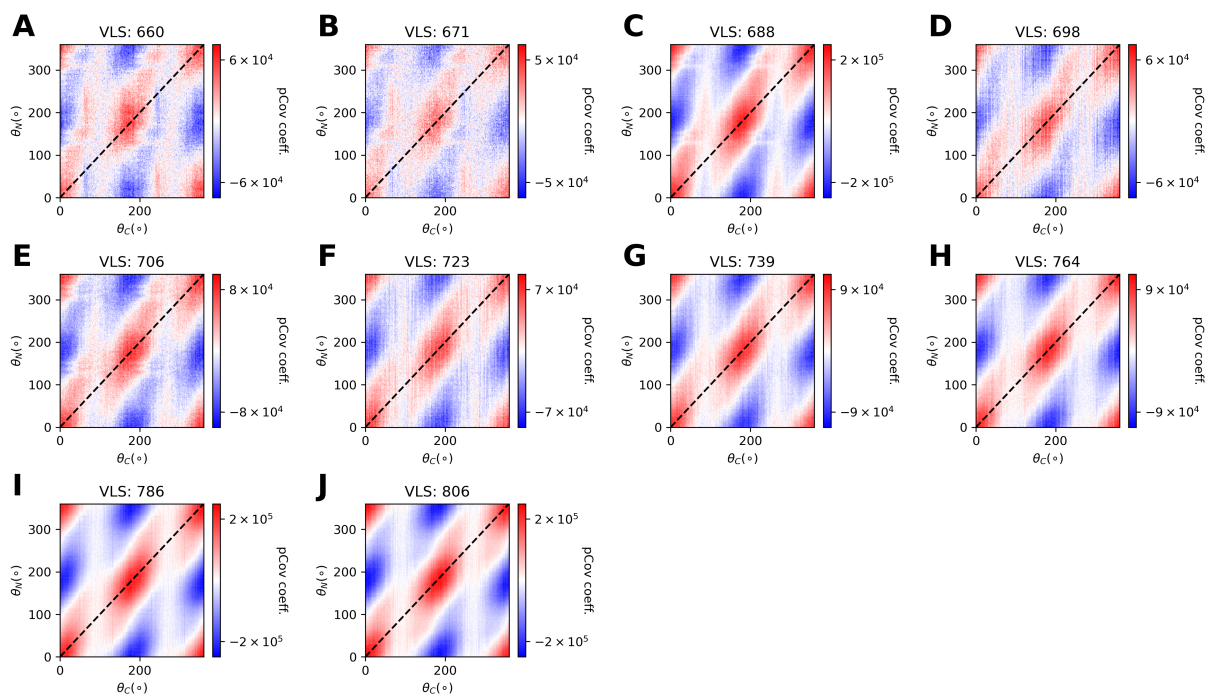


Figure S5: Partial covariance maps calculated on *s*-triazine data. The false-color map in each panel shows the partial covariance map calculated on streaked *c*-VMI data with VLS centroids in a certain bin. The title of each panel shows the mean value of VLS centroids of data in this bin.

For each dataset, we calculate the spectral center-of-mass of each single shot, and bin these data into 2 groups based on the spectral centers-of-mass. For data in each group, we calculate a 2-D partial covariance map based on Eq. S4. Figures S3, S4 and S5 show partial covariance maps for all delay points from pyridine, pyrimidine and *s*-triazine data. When the X-ray central photon energy is close to the nitrogen K-edge, the asymmetry parameter β_2 (see Sec. 2.3) of the N-1s photoemission feature is close to 0. The angular distribution of the N-1s photoemission feature is approximately isotropic, and all partial covariance maps therefore do not have a $\cos^2 \theta_N$ shape along the θ_N -axis. On the other hand, the C-1s photoemission features in all datasets have above 100 eV kinetic energies and their asymmetry parameters β_2 are always close to 2. The angular distribution of the C-1s photoemission feature therefore has a dipolar shape, and the shapes of all partial covariance maps are modulated by a $\cos^2 \theta_C$ feature along the θ_C -axis.

We extract the photoionization delays by focusing on the best-correlated area on partial covariance maps. Every such partial covariance map has a high-value area (i.e. the area with the best joint variability) around the diagonal line $\theta_N = \theta_C$. When the XFEL central photon energy gradually decreases to the nitrogen K-edge (i.e. smaller value in VLS center of mass), the most correlated area in partial covariance maps gradually deviate from the diagonal line and moves to $\theta_N = \theta_C + \Delta\vartheta$. This diagonal shift feature in the partial covariance map has an intuitive interpretation. Given a photoionization delay $\Delta\tau = T_L \times \Delta\vartheta/2\pi$, the N-1s photoemission feature is streaked to $\theta + \Delta\vartheta$ when the C-1s photoemission feature is streaked to θ , no matter what the detector angle θ is. Therefore, the streaking-induced signal change at $\theta + \Delta\vartheta$ in the N-1s photoemission feature has the best joint variability with the streaking-induced signal changes at θ in the C-1s photoemission feature.

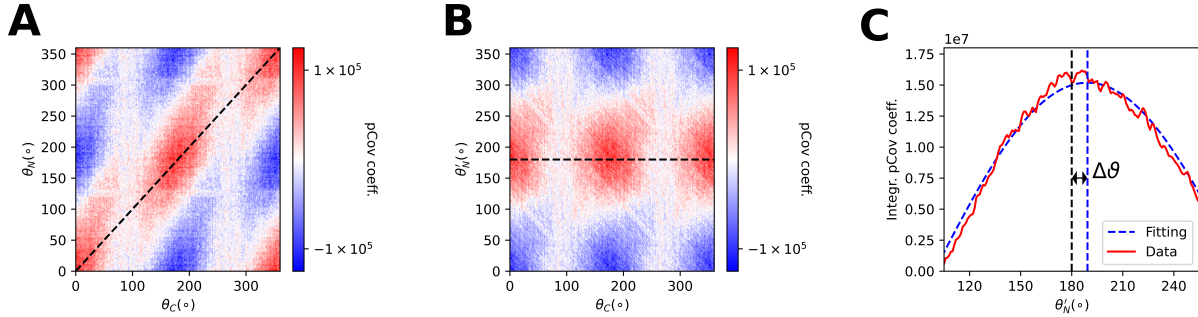


Figure S6: Demonstration of fitting photoionization delay on partial covariance map. Panel (A) shows the partial covariance map calculated on pyrimidine data at XFEL central photon energy 410 eV, which is the same as Fig. S4(C). Panel (B) shows the rolled map of the partial covariance map in panel (A). The diagonal line is rolled to horizontal. The most correlated region, demonstrating the photoionization delay, clearly deviates from the horizontal line at 180° . Panel (C) shows the 1-D trace by integrating the rolled map in panel (B), and its sine fitting. The maximum of the 1-D trace deviates from 180° by approximately 8° , which corresponds to approximately 100 as in photoionization delay.

We extract the photoionization delay from the diagonal shift feature in partial covariance maps. As shown in Fig. S6, panels (A) and (B), we first rotate the $\text{pCov}[\tilde{X}(\theta_C), \tilde{Y}(\theta_N); I(\omega)]$ into another map $\text{pCov}[\tilde{X}(\theta_C), \tilde{Y}(\theta'_N); I(\omega)]$ by using the transformation $\theta'_N = \theta_N - \theta_C + 180^\circ$. By comparing Fig. S6(B) to Fig. S6(A), the diagonal line in Fig. S6(A) becomes the horizontal line in Fig. S6(B). As a result, the

photoionization-delay-induced diagonal shift in Fig. S6(A) results in a vertical shift in Fig. S6(B). We then integrate along the θ_C -axis of the rolled partial covariance map to get an 1-D trace $f(\theta'_N)$. The integration is taken on $\theta_C \in [-75^\circ, 75^\circ] \cup [105^\circ, 255^\circ]$ to avoid the nodes along the θ_C -axis. Such an integration is valid since the N-1s photoemission feature is almost isotropic. In the last step, we perform a sine fitting on the 1-D trace $f(\theta'_N)$. We extract an angular shift $\Delta\vartheta$ between the peak of the sine fitting curve and $\theta'_N = 180^\circ$. The value of $T_L \times \Delta\vartheta/2\pi$ is used as the photoionization delay in the partial covariance analysis.

We use a bootstrapping approach to estimate the error in the covariance analysis of photoionization delays. For each delay point, we perform 100 times of resampling with replacement on data in this group to generate 100 unique datasets. For each generated dataset, we perform the aforementioned partial covariance analysis procedure and extract a photoionization delay. The errorbar of each delay point shown in Fig. 3(A) in the main text represents 3 times the standard deviation of 100 delays generated from the bootstrapping method.

2.2.2 Center-of-mass analysis

As a complementary method, we developed the center-of-mass (CM) analysis, which also extracts photoionization delays from our experimental measurements. Here, we demonstrate the method based on pyrimidine at an XFEL central photon energy of approximately 417 eV, which corresponds to three separate runs, where each run contains about 34000 shots.

The central energy and pulse intensity can be characterized by fitting the VLS spectra with a Voigt profile, as demonstrated in Fig. S7, where the center of the peak is fixed at the center of mass (CM) of the spectrum. Within the same run, the shot-to-shot central wavelength and intensity change is not negligible. Therefore, intensity selection, central-wavelength grouping, and shot-to-shot electron kinetic energy adjustment are performed.

The kinetic energy of both C-1s and N-1s electrons increases as the photon energy increases, which leads to its projection on the c-VMI with a greater radius. Here we use the C-1s electron for the VLS-radius calibration, where a clear falling edge is visible, and its position can be determined by the greatest gradient, as shown in Fig. S8. Within the same run, the relation between the VLS CM and the C-1s radius can be approximated by a linear function.

When the X-ray and the IR are spatially and temporally overlapped, the streaking effect causes the shift of the electron distribution on the c-VMI, which increases the signal beyond the radius determined by the shots in which X-ray and IR pulses were not temporally overlapping. Therefore, the CM of the ring region outside the C-1s radius, which is shot-to-shot calibrated according to the single-shot VLS spectrum, is sensitive to the streaking direction. Figure S9 demonstrates the principle with a relatively strongly streaked shot, where its differential plot subtracted by the averaged unstreaked image reveals the increase of the signal in the ring region. The ratio between the ring-region signal and the full-image signal can be used as a parameter to characterize the strength of streaking.

The single-shot intensity can be characterized by both GMD and VLS peak amplitude. The distributions are compared in Fig. S10, where a clear correlation can be found. For each run, shots with GMD and VLS amplitude between 40% and 90% are selected, in order to exclude the images with too weak signal, where the noise level is relatively high, as well as images with too strong signal, which may suffer from the detector saturation. The CM distributions before and after the GMD and VLS amplitude selections are compared in Fig. S11. Since the CM fitting is less stable with weaker signal, the

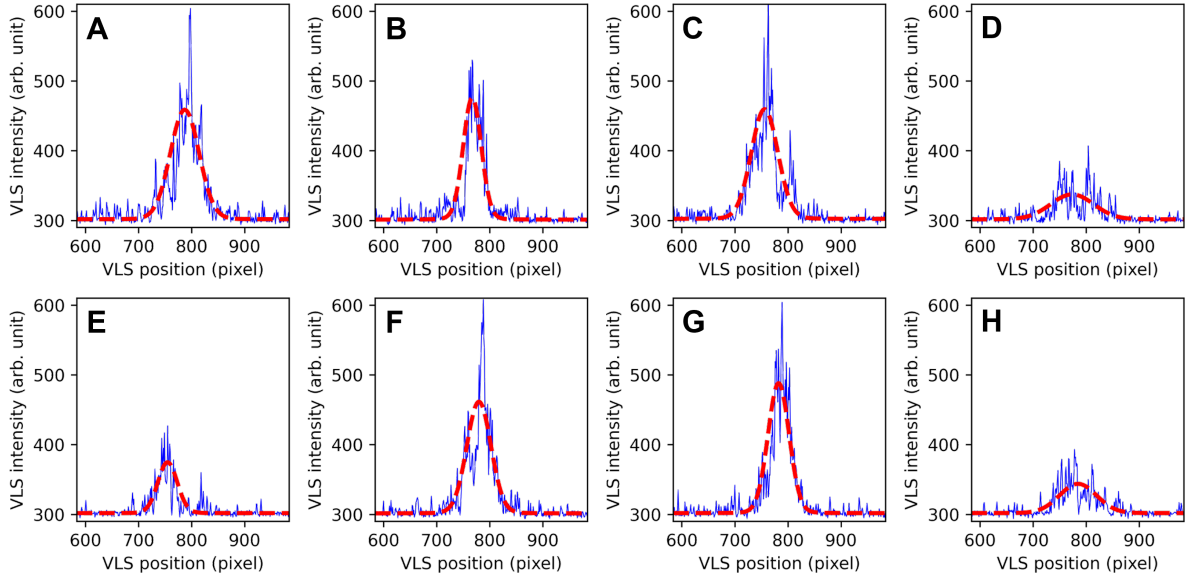


Figure S7: VLS spectra of 8 randomly chosen shots in the same run. The blue solid curve is the original signal, while the red dashed curve is the fit, the center of which is fixed to the CM of the corresponding spectrum and the shape is determined by the Voigt fitting.

distributions without selection shows some random scattering feature. The X-ray-IR unoverlapped (bkg) CM after selection has a circular distribution, which corresponds to the random error of the CM fitting, while the X-ray-IR overlapped (stk) CM after selection shows larger shifts in both x - and y -directions with an elliptical distribution, which corresponds to the dipole distribution of the C-1s electron. A distinct separation between the weakly and strongly streaked shots is possible with the streaking-strength parameter defined as the ring-region signal divided by the full-image signal. As shown in (H) and (I) in Fig. S11, the stk distribution contains one part that is similar to the bkg distribution which corresponds to the weakly streaked shots and another part that is above the threshold (95% of bkg) and corresponds to a significant proportion of electrons moving into the ring region. This threshold is used as another criterion for shot selection.

Applying the selection rules mentioned above, one gets an elliptical distribution whose central part is also elliptical, as shown in Fig. S12 (B), instead of the circular feature in Fig. S11 (D) that corresponds to the contribution of the weakly streaked shots. In order to retrieve the streaking direction, a factor of $\text{std}(\Delta y)/\text{std}(\Delta x)$ is multiplied by Δx , so that the elliptical distribution is stretched into the circular distribution, and the streaking direction can be inferred, as shown in Fig. S12. The retrieved streaking direction is almost uniformly distributed after the correction, which agrees with the physical insight that the X-ray-IR time delay jitters randomly across the 2π -phase.

In order to obtain the relative time delay between the C-1s and N-1s electrons, the phase analysis is performed with the shots grouped according to the determined streaking direction, as illustrated in Fig. S13. In (A-C) the subtle shift of the electron within a group can be visualized by the differential plot subtracting the average of all streaking directions, as compared in (D-F), where one can find the C-1s electron shifted towards the streaking direction, causing a positive edge in the differential plot and

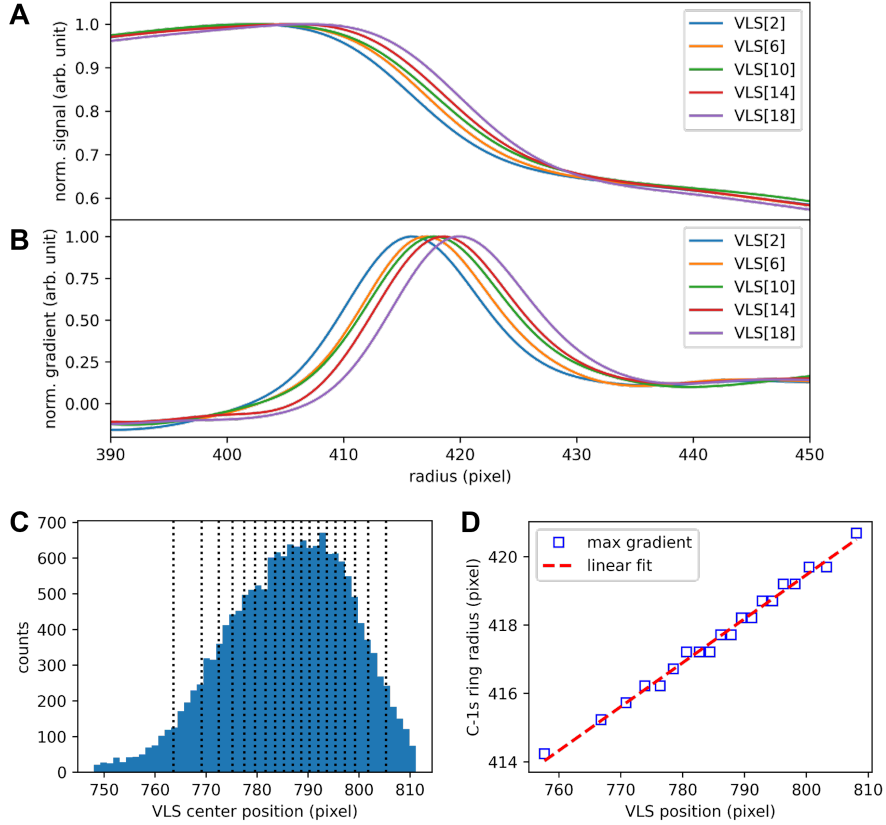


Figure S8: VLS-radius calibration by the X-ray-IR temporally unoverlapped shots. (A) The normalized signals near the C-1s edge for various VLS bins. (B) The normalized gradients (reversed) of the corresponding signals in (A). (C) The histogram of the VLS center positions for the run, where the dotted vertical lines indicate the division of the VLS bins. (D) The VLS-radius calibration. The blue squares correspond to the centers of the VLS bins and the corresponding maximal-gradient radii, which has a minimal increment of 0.5 pixel, while the red dashed line corresponds to the linear fitting using all the VLS bins except the first and the last bins.

a negative edge in the opposite direction. The N-1s electron overlaps with the ATI electron from the valence shell in the inner part of the image. However, since the ATI electron distribution is insensitive to the relative time delay between X-ray and IR, the differential plots exclusively manifests the shift of the N-1s photoelectron. We note that fixing the streaking direction and investigating the signal counter-clockwise on the electron edge is equivalent to fixing a position on the electron edge and investigating the signal variation while rotating the streaking direction clockwise, while the latter has an advantage that the phase is unaffected by the inhomogeneity of the detector. For example, by fixing two boxes at the N-1s and C-1s edges, as illustrated in Fig. S13 (H), one obtains the oscillating signals as functions of the streaking angle ϑ , as plotted in Fig. S13 (J) and (K) for the summed data and individual data from each run, respectively, where the relative time delay between N-1s and C-1s can be extracted by

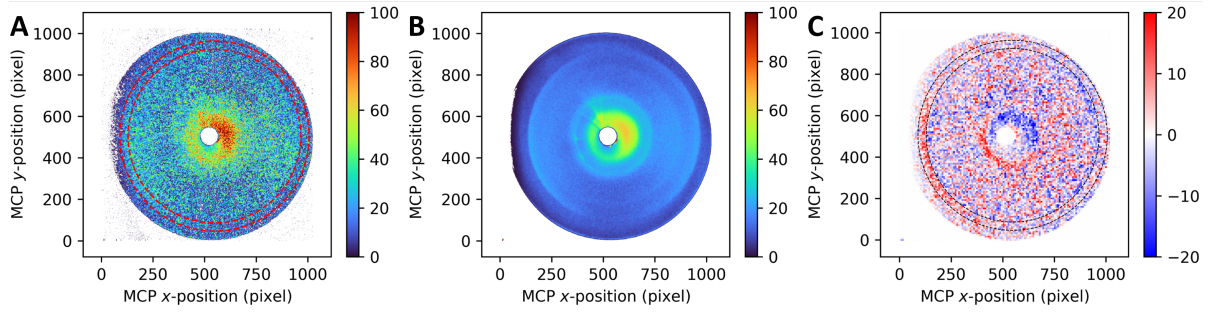


Figure S9: Principle of CM fitting. (A) A typical single-shot image at 416.4 eV, where the CM is taken within the area between the two dashed circles. (B) Average image of the X-ray-IR unoverlapped shots. (C) Differential image of (A) subtracted by (B). The image is binned and averaged by 8×8 pixels to reduce fluctuation. The dashed circles correspond to the ones in (A).

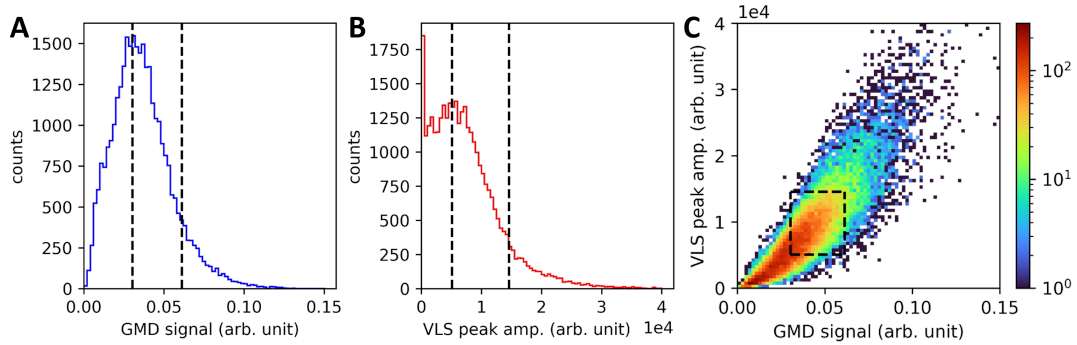


Figure S10: Shot selection based on GMD and VLS amplitude. (A) Distribution of the GMD signal. The vertical dashed lines correspond to 40% and 90% of the distribution, between which the shots are selected. (B) Distribution of the integrated VLS peak fitted as shown in Fig. S7. The vertical dashed lines correspond to 40% and 90% of the distribution, between which the shots are selected. (C) The two-dimensional histogram of the GMD signal and the VLS peak amplitude, where the selection criterion is indicated by the black dashed box.

fitting the phases of the cosine-like oscillations. The same procedure is repeatedly performed at various detector angles, and the average delay and the uncertainty can be determined.

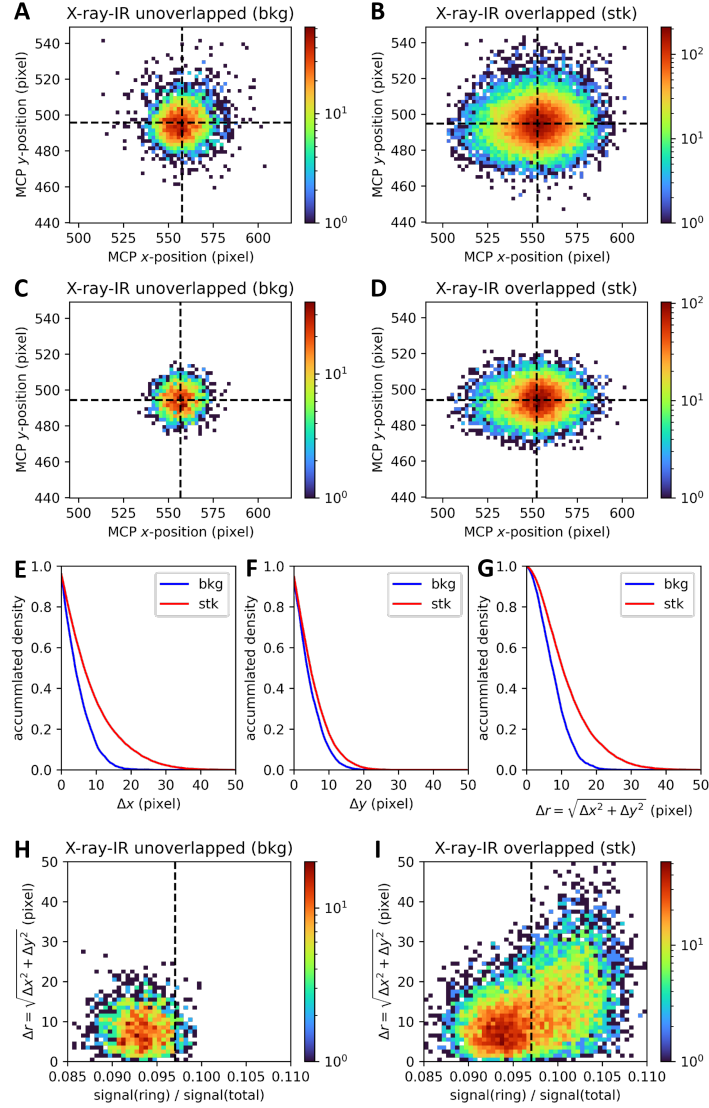


Figure S11: CM distributions of the X-ray-IR temporally unoverlapped (bkg) shots and the X-ray-IR temporally overlapped (stk) shots. (A,B) CM distribution of the whole run. (C,D) CM distribution of the run after GMD and VLS-amplitude selections. The black dashed lines in (A-D) indicate the average CM in x - or y -dimension. (E,F,G) Accumulated density of the CM shift (the vertical value corresponds to the proportion of shots with CM shifts smaller than indicated by the horizontal value) regarding Δx , Δy , and $\Delta r = \sqrt{\Delta x^2 + \Delta y^2}$. The GMD and VLS-amplitude selections are applied. (H,I) Ratio between the ring-region defined in Fig. S9 and the full image. The vertical dashed lines correspond to the 95% level of the bkg shots, which is used as the threshold of streaking-strength selection.

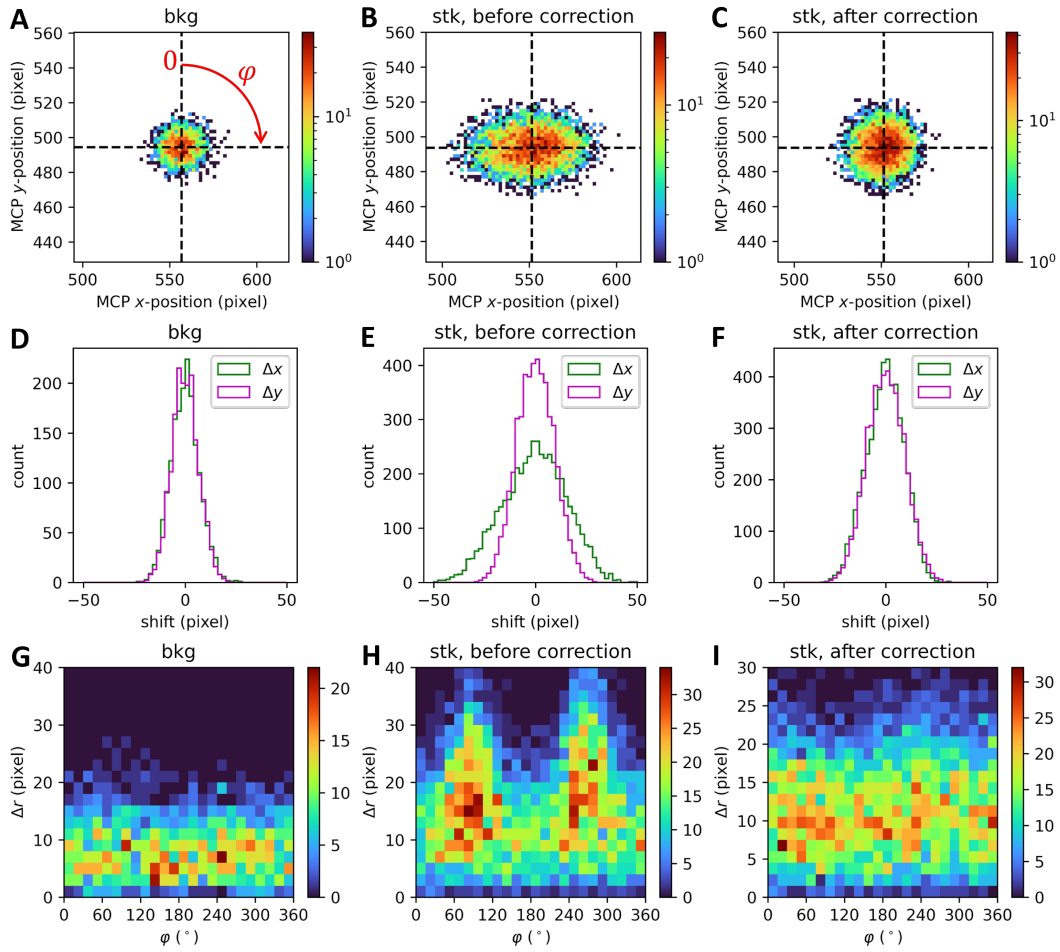


Figure S12: Dipole correction and streaking-direction determination. The GMD and VLS-amplitude selections and the streaking-strength selection are applied. (A) CM distribution of bkg. (B) CM distribution of stk before dipole correction. (C) CM distribution of stk after dipole distribution. (D,E,F) The x - and y -projections of the corresponding CM distributions. (G,H,I) CM distribution in the polar coordinates corresponding to (A-C), where the azimuth angle is defined as indicated in (A).

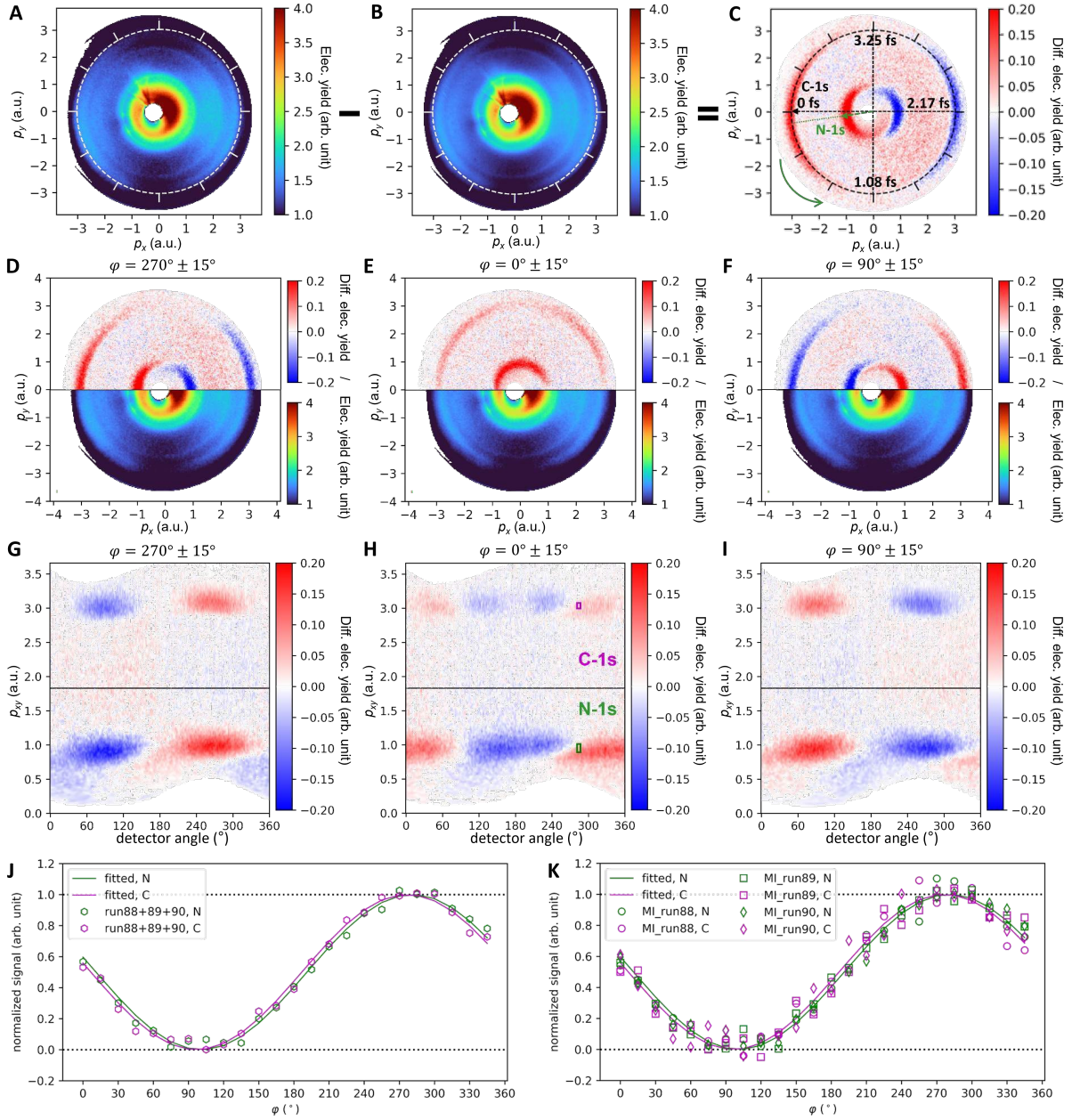


Figure S13: (Caption on the following page.)

Figure S13: Illustration of the center-of-mass analysis method for the extraction of the photoionization delays. (A) Averaged image of stk shots with determined streaking angle between $270^\circ \pm 15^\circ$. (B) Averaged image of stk shots with all streaking angles. (C) Differential image between (A) and (B). (D,E,F) The averaged streaked images at different streaking angles ϑ sorted by post-selection, where the lower panels correspond to the original images, whilst the upper panels are subtracted by the averaged image over all streaking angles. The images are normalized to arbitrary unit, while the normalization is consistent between the original and the differential images. (G,H,I) Differential images converted into the polar coordinates, with the upper and lower panels corresponding to the C-edge-corrected and N-edge-corrected images, respectively. (J) Signal variation as a function of the streaking angle ϑ at a fixed area on the detector indicated by the green box for N-1s and the magenta box for C-1s in (H). The signals are normalized and subtracted by the mean value. The curves correspond to the cosine fitting. (K) Same as (J) but the markers correspond to three individual runs with independent data processing, while the three runs are summed in (A-J).

2.2.3 Comparison of the two methods

We are now in the position to compare these two independent methods of extracting photoionization delays – the partial covariance and the center-of-mass method. Figure S14 directly compares the photoionization delays by showing the results of the partial-covariance method with filled symbols and those of the center-of-mass method with empty symbols. The results from the two methods agree very well, practically always within the respective error bars. Since the error bars of the partial-covariance method are smaller, particularly in the case of *s*-triazine, we have chosen to show those data in the main text.

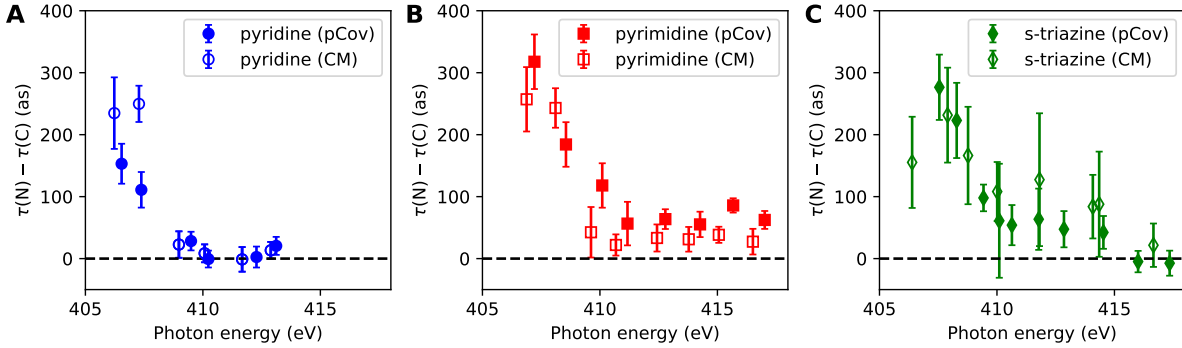


Figure S14: Comparison of the extracted time delays with the partial covariance analysis (pCov) and the center-of-mass method (CM). (A) Pyridine (B) Pyrimidine (C) *s*-triazine.

2.3 Determination of Photoelectron Asymmetry Parameters

We perform a covariance analysis to extract the photoelectron asymmetry parameter β_2 as a function of x-ray photon energy for pyridine, pyrimidine, and *s*-triazine. The data analysis of β_2 is performed on unstrained c-VMI images.

In the first step, we calculate the simple covariance $\text{Cov}[M(p_x, p_y), I(\omega)]$ between the c-VMI pixel value $M(p_x, p_y)$ and the VLS pixel $I(\omega)$. Given a X-ray photon energy $\hbar\omega$, the 2-D covariance map $\text{Cov}[M(p_x, p_y), I(\omega)]$ as a function of (p_x, p_y) contains the X-ray-photon-energy-dependent features of C-1s and N-1s photoelectrons. The signal from Above Threshold Ionization (ATI) is removed in these 2-D covariance maps, because ATI electrons were generated by the streaking laser and not correlated with X-ray photon energy. The white noise in c-VMI images is removed in the simple covariance maps. In the practical data analysis procedure, we calculate the simple covariance between the c-VMI pixel value $M(p_x, p_y)$ and VLS slices of 10 VLS pixels each to improve the signal-to-noise ratio. The covariance maps calculated on pyrimidine data are shown in Figure S15. From panels A to I in Fig. S15, radii of both photoemission features gradually decrease (i.e. lower kinetic energy) when using the VLS slice with smaller value (i.e. lower X-ray photon energy) to calculate 2-D covariance maps.

These 2-D covariance maps still contain some unwanted features that are not parts of C-1s and N-1s photoemission features and are detrimental to our analysis of β_2 . For example, we can observe a uniform background in each panel of Fig. S15. This uniform background comes from carbon and nitrogen K-edge Auger-Meitner electron yield. The simple covariance map $\text{Cov}[M(p_x, p_y), I(\omega)]$ still

contains signals from Auger-Meitner electron yield because Auger-Meitner electron yield depends on X-ray pulse energies. For the same reason, these simple covariance maps $\text{Cov}[M(p_x, p_y), I(\omega)]$ also contains X-ray artifacts, which appear as sharp rings with the same shapes in every panel of Fig. S15.

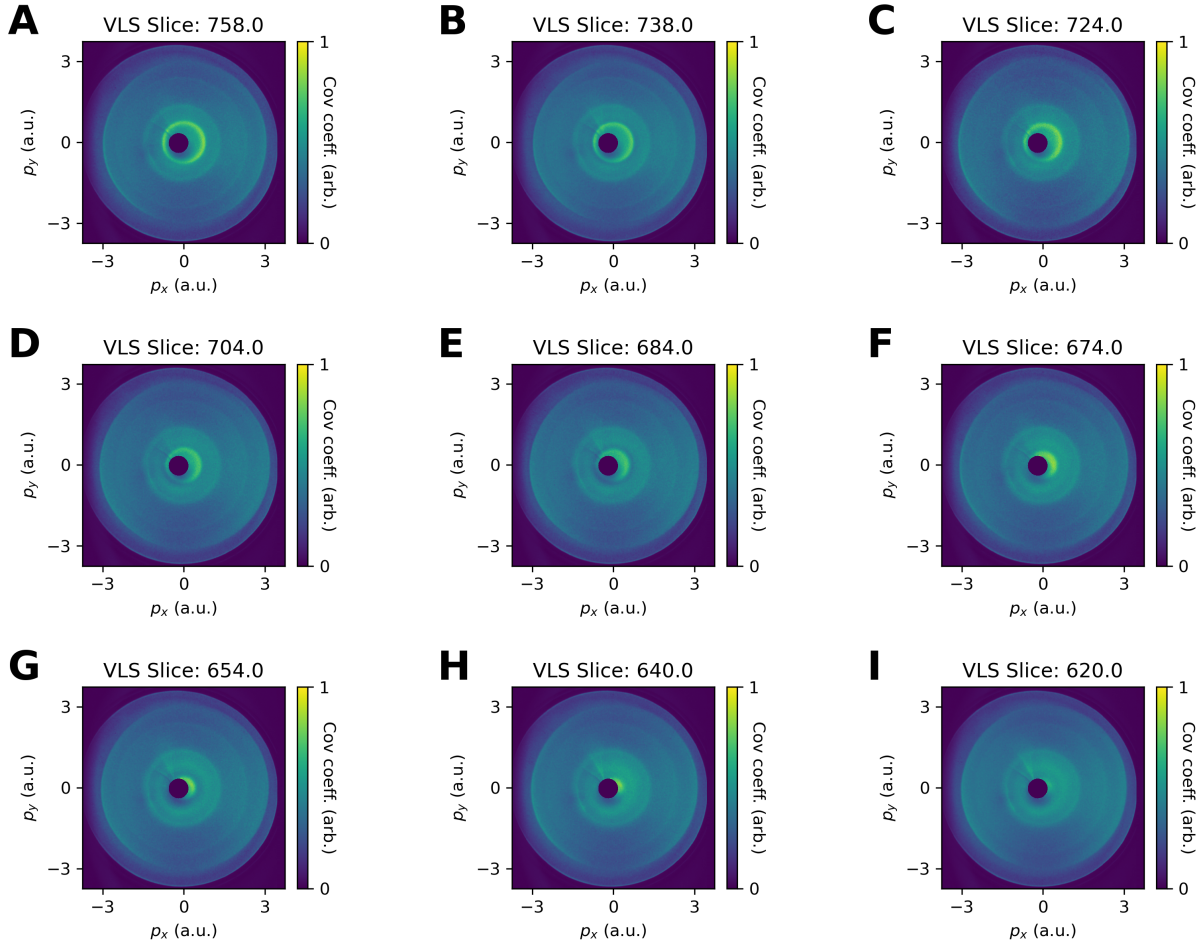


Figure S15: Covariance maps calculated between c-VMI pixels and VLS slices. Panels (A)-(I) represent covariance maps calculated on pyrimidine data. The title of each panel labels the center of the VLS slice (i.e. uncalibrated X-ray spectrum) used in the calculation of the covariance map in this panel.

To better extract β_2 from these simple covariance maps, we utilize the fact that both the Auger-Meitner electron yield and the X-ray artifacts do not sensitively depend on the X-ray photon energy. To this end, we calculate the differential map between 2 covariance maps calculated with adjacent VLS slices after appropriate normalization. By calculating such a differential map, we can remove contributions from the Auger-Meitner electron yield and the X-ray artifacts. The resultant differential map only contains the differential traces of C-1s and N-1s photoemission features. By applying an inverse Abel transform to the differential map, we can retrieve two 1-D traces, namely $\Delta I_0(p_r)$ and $\Delta I_2(p_r)$, from the differential map. Since $\Delta I_0(p_r)$ and $\Delta I_2(p_r)$ are retrieved from a differential map, they contain both positive and negative features. To avoid the singularity in calculating $\int \Delta I_2(p_r) / \int \Delta I_0(p_r)$, we fit the

value of β_2 by minimizing the following objective,

$$f(\beta_2) = \int_{\text{ROI}} dp_r (\Delta I_2(p_r) - \beta_2 \Delta I_0(p_r))^2, \quad (\text{S5})$$

which is equivalent to a linear regression between $\Delta I_0(p_r)$ and $\Delta I_2(p_r)$ with the bias term set to 0.

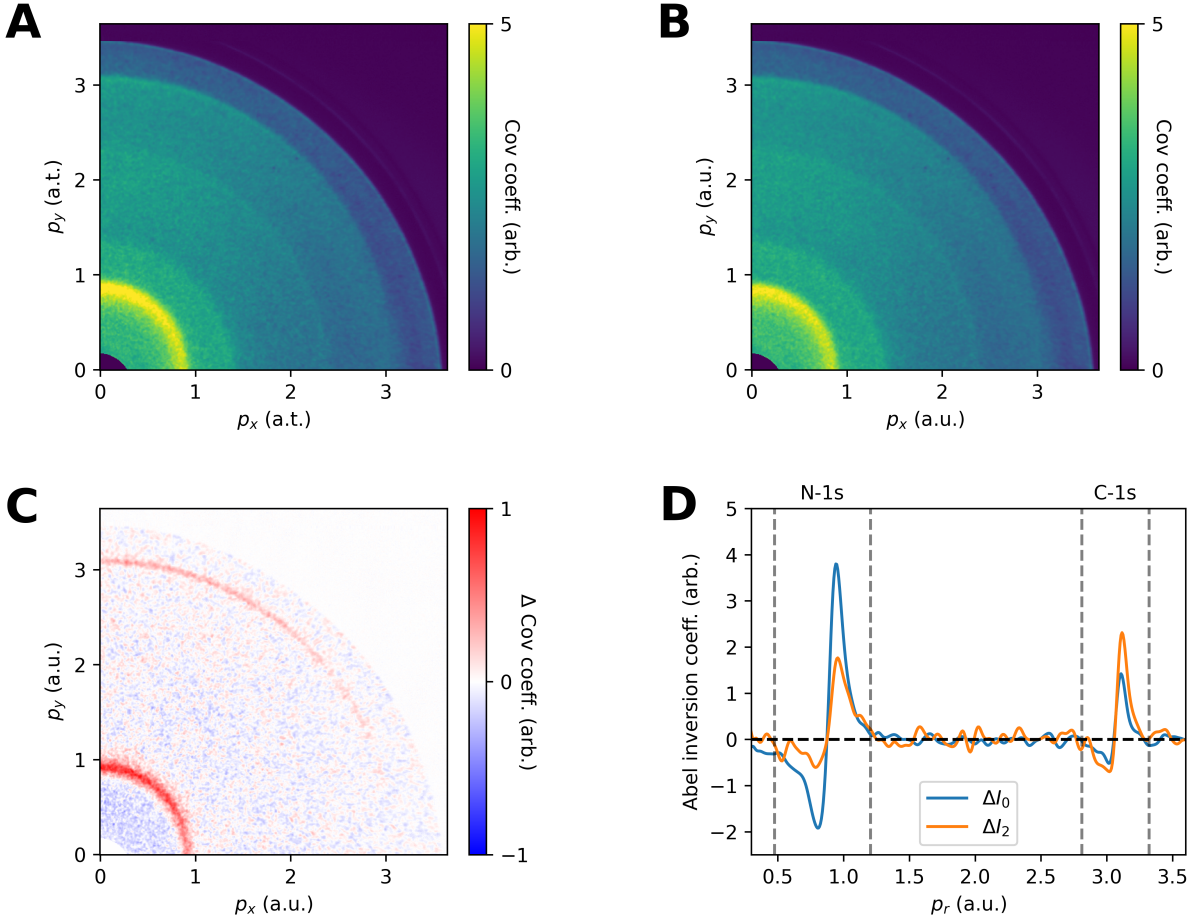


Figure S16: Use of the relative difference in covariance maps to determine β_2 . Panel (A) shows the covariance map calculated with the VLS slice at 812. Panel (B) shows the covariance map calculated with the VLS slice at 802. Panel (C) shows the differential map between panels A and B. Panel (D) shows the inverse Abel transform of the quadrant shown in panel C.

When the X-ray central photon energy is around 450 eV, all four quadrants of c-VMI images are complete and can be used in the photoelectron asymmetry parameter analysis. We calculate the values of β_2 on all four quadrants separately. The average of β_2 calculated on four quadrants is used as the mean value, and the standard deviation of β_2 calculated on four quadrants is used as the error. When the X-ray central photon energy is close to the nitrogen K-edge, only the top right quadrant (orientation shown in Fig. S15) is used in the photoelectron asymmetry parameter analysis. The errorbars of N-1s β_2 from 407 eV to 418 eV are taken from the numerical uncertainty of the fitting in Eq. S5.

3 Theoretical Methodology

3.1 Core-level photoionization calculations

The N $(1s)^{-1}$ photoionization of the three azabenzenes considered here were studied using two methods, the basis-set complex Kohn method (40) and ePolyScat (41, 42). The ePolyScat calculations used a static-exchange potential that was modified by the addition of an approximate local potential that represented the correlation and polarization interactions felt by the emitted photoelectron due to its interaction with the residual ion of the molecule (43). The one-electron basis set used to obtain the occupied molecular orbitals was a correlation consistent valence triple zeta (44) and the geometry used minimized the Hartree-Fock energy. For the systems with equivalent N-atoms, a one-channel localized hole calculations from ePolyScat were found to be equivalent to calculations where the ionization from the different the N $(1s)^{-1}$ holes were coupled together in a multichannel calculation using the complex-Kohn method (45) as seen in Fig. S17A for the ionization of *s*-triazine. The orientation-averaged one-photon time delays are also seen to be nearly the same for these two calculations in Fig. S17A. In all calculations the initial state and in the ionized state were constructed using the same set of orbitals. The positions of the resonances in the photoionization cross sections were sensitive to the orbitals used in the calculation. In Fig. S17B we compare the cross section for *s*-triazine using the orbitals from the neutral initial state, orbitals from a calculation where the open shell ion state with an N $(1s)^{-1}$ vacancy is localized on one of the N-atoms, and orbitals from an equivalent-core calculation (46). Additionally, we have plotted the cross section where we have added a correlation-polarization (CP) potential to the equivalent-core calculation and scaled the CP potential by a factor of 2.0. This shifted the position of the largest resonance to an energy that agrees with the peak in the experimental absorption cross section (47). In Fig. S22 we can see that the same CP potential shifts the peak seen in the N $(1s)^{-1}$ ionization in all three molecules considered here to agree with experimental absorption cross sections (47).

3.2 Characterization of the resonances above the N K-edge of the azabenzenes.

In the photoionization calculation, we found evidence of several shape resonances in each molecule. The partial cross sections for each irreducible representation and each of the three molecules considered here are presented in Fig. S18. In the orientation of the molecules used here, for pyridine and *s*-triazine in the equivalent-core approximation, the molecules have C_{2v} symmetry so that the orbitals with A_1 and B_1 symmetry are σ type orbitals in the plane of the molecule and the B_2 orbitals are π orbitals with a node in the plane of the molecules. For pyrimidine in the equivalent core approximation the system has C_s symmetry so the A' orbitals are σ orbitals and the A'' orbitals are π orbitals. Immediately we see that there are no π resonances in the continuum. In pyridine, there are two noticeable resonances below 430 eV with the lower one, around 410 eV, having a peak cross section in the $L = 2$ partial wave, where the upper resonance near 420 eV has a peak cross section in the $L = 5$ partial wave. In B_1 symmetry, the lower resonance near 408 eV has significant contributions from $L = 5$ whereas the higher resonance has a significant contribution from $L = 6$. In the cross sections for pyrimidine, there are again resonances around 409 eV and 420 eV, but due to the lower symmetry in this system it is difficult to distinguish the different resonances in the partial-wave analysis. In *s*-triazine, the A_1 symmetry cross section again has two clear resonances, however in this case the upper resonance has a lower energy, at about 415 eV, compared to the upper resonance in the B_1 symmetry resonances. In the B_1 partial cross sections, the

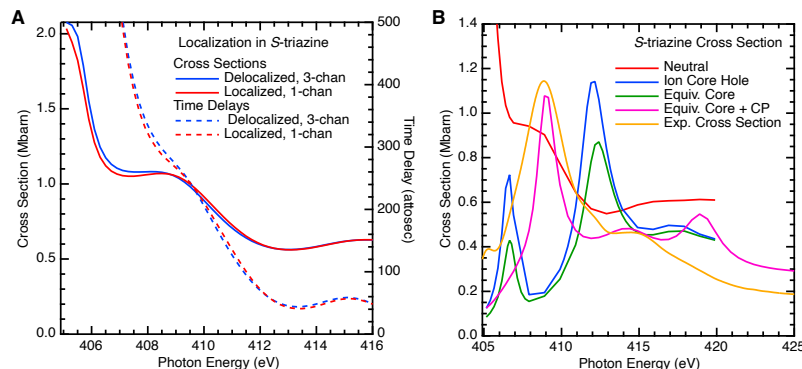


Figure S17: Approximations used in the computation of the core-level photoionization calculations. (A) Difference between a three-channel calculation of the $N(1s)^{-1}$ photoionization using a three-channel calculation for ionizing the three nearly degenerate $N(1s)^{-1}$ hole states of *s*-triazine using delocalized Hartree-Fock orbitals of the neutral molecule (blue lines) and a one-channel photoionization calculation using a core orbital localized on one N-atom. (B) Total photoionization cross section of *s*-triazine computed with different choices of the orbitals used: localized neutral orbitals (red), orbitals from an open-shell Hartree-Fock calculation on the ion with a vacancy on one of the N-atoms (blue), orbitals obtained from an equivalent-core calculation (green), orbitals obtained from an equivalent-core calculation with an added correlation-polarization potential (pink), and experimental absorption data (47) (tan).

lower resonance has the largest contribution from the $L = 5$ partial waves and the upper resonance has the largest contribution in the $L = 6$ partial wave.

To analyze these shape resonances in more detail, we performed calculations to obtain the position and wave functions of the resonant states directly. In these calculations we used a local approximation to electron-molecule interaction potential where the exchange potential was replaced by the free-electron-gas exchange (FEGE) potential, using a fixed scattering energy of 15 eV in the computation of the exchange potential (42, 48). Using the static potential, plus the FEGE exchange potential, plus the CP potential, truncated at a fixed r of 8.5 Å, which is the distance from the center of the molecule to where the magnitude of the orbitals are less than 10^{-6} in atomic units. We then solved the scattering equations at complex energies with negative imaginary parts on the unphysical sheet, i.e. $\text{Im}(k) < 0$, where k is the complex-valued momentum of the photoelectron, to locate the poles of the S -matrix. The wave functions at the poles will then have only outgoing flux, unlike wave functions at real energy which have both incoming and outgoing flux. These states which are Siegert states with a cutoff potential, also known as Kapur-Peierls eigenstates (49–51), are then used to visualize resonances including the location of the resonance on the molecule and their angular momentum composition which can indicate the mechanism for trapping the metastable resonance state. These wavefunctions have the asymptotic form $\exp(ikR) = \exp(ik_r R) \exp(ik_i R)$, where $k_r = \Re k$, $k_i = \Im k$. This explains their divergence at large R seen in Fig. 5 of the main text and in Fig. S21 below.

The location of the poles found using the Kapur-Peierls method for the three molecules considered are shown in Fig. S19. Each plot shows many poles along a line, which correspond to non-resonant scattering (50) and some poles located closer to the real energy axis away from this line which correspond to resonances. In Fig. S19 we have circled five poles for each molecule which are well separated from

the non-resonant scattering poles. Although the treatment of exchange is different in the pole-search results shown in Fig. S19 and calculated cross sections in Fig. S18, there is a very good correspondence between the resonance features in cross sections given in Fig. S18 and the location of the resonance poles identified in Fig. S19.

For each pole shown in Fig. S19, in Fig. S20 we plot the absolute square of the resonance wave function in the plane of the molecule. For each molecule, the orientation of the molecule has the N-atom which is ionized on the right-hand side of the plots. In each case, the resonance wave function only contains outgoing waves, so that if one were to extend these plots to larger distances from the molecule, the wave functions would grow exponentially. The plots then indicate the part of the wave functions where the electron is trapped by angular momentum barriers around the region of the molecule. The leftmost column contains the wave function for the strong resonances which occur near threshold. It is apparent that the strength of these resonances is due to the fact that the resonant state has a large amplitude at the N-atom which was ionized. In contrast, resonances in the right-hand column have very little amplitude near where the ionized N-atom is located leading to the absence of this resonance in the computed cross sections shown in Fig. S18. The next-to-the-last column on the right-hand side gives the resonant wave functions for the well isolated resonances occurring at a photon energy of 417 eV which corresponds to a photoelectron kinetic energy of 12 eV. These resonances clearly have a nodal structure corresponding to $L = 6$ in agreement to the partial wave contributions to the cross sections shown in Fig. S18.

As an alternative to the qualitative analysis of the resonance wave functions shown in Fig. S20, one can also plot the absolute square amplitudes of the partial-wave radial functions, as given in Fig. S21. In this figure, for a given value of L , the square amplitudes of all the radial wave functions are given. The most important radial wave functions are then highlighted using color. The resonances in the left column clearly show resonance wave functions which are primarily trapped in an $L = 5$ angular momentum barrier from which the electron tunnels leading to a large amplitude in the $L = 5$ photoionization amplitude. In a similar fashion, the resonances shown in the next-to-last column on the right show $L = 6$ resonances which then tunnel through the corresponding angular momentum barrier leading to strong $L = 6$ photoionization amplitudes as seen in Fig. S18.

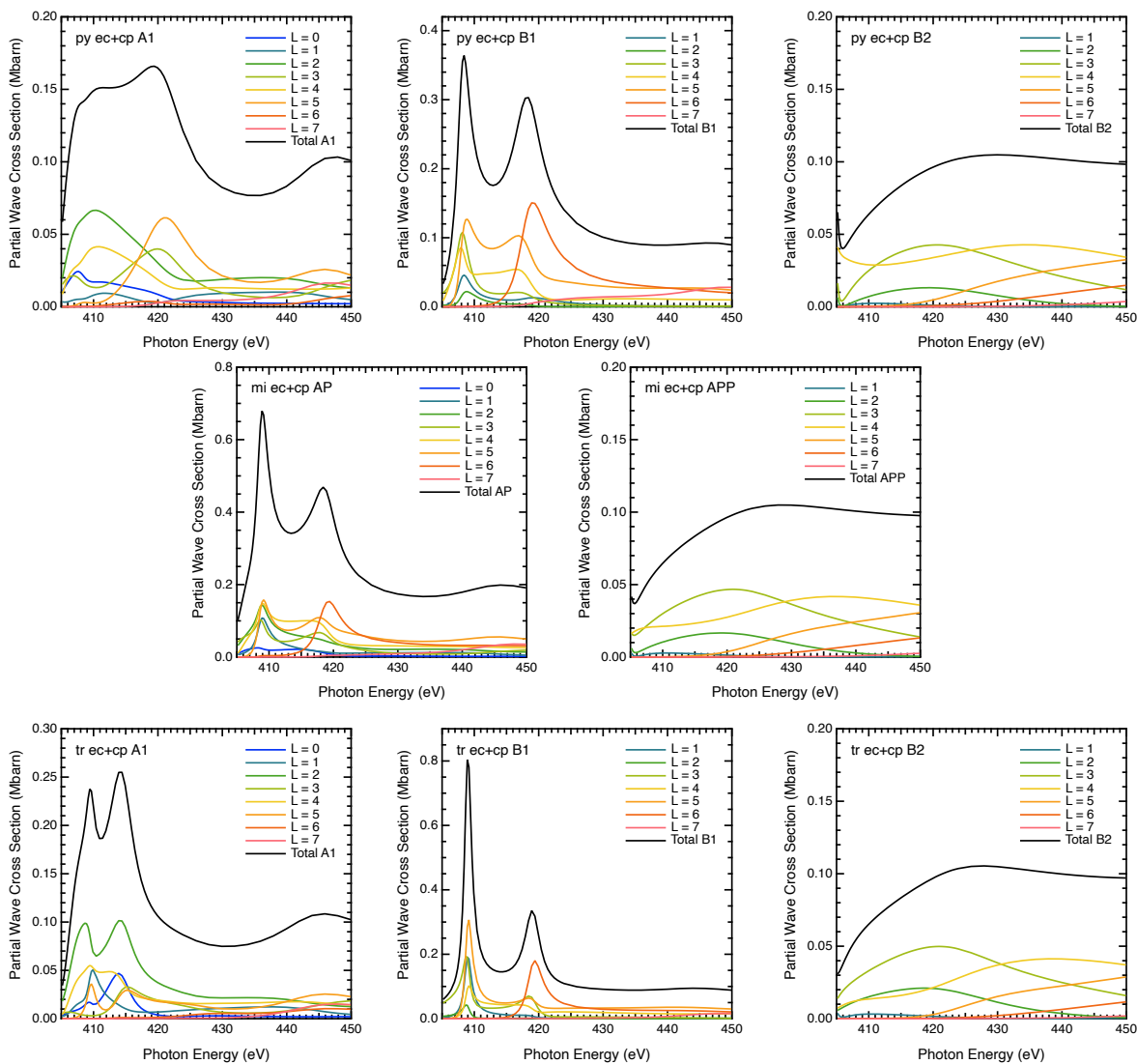


Figure S18: Decomposition of the total photoionization cross section above the nitrogen K-edge, calculated with the CP method, into the partial-wave cross sections of each dipole-accessible irreducible representation in the point groups of the single-site ionized azabenzene molecules. (top) pyridine with C_{2v} irreps A_1 , B_1 and B_2 , (middle) pyrimidine with C_s irreps A' and A'' , (bottom) *s*-triazine with C_{2v} irreps A_1 , B_1 and B_2 .

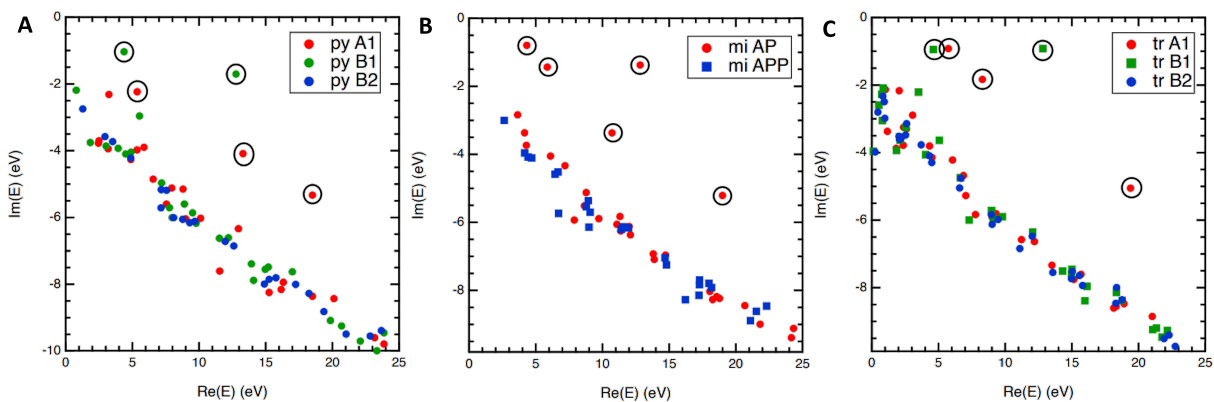


Figure S19: S -matrix pole locations of (A) pyridine, (B) pyrimidine and (C) s -triazine in the vicinity of the nitrogen K -edge. The resonance positions are identified with circles. The legends indicate the molecule and the dipole-accessible irreps in the point group of each single-site-ionized molecule (C_{2v} for pyridine and s -triazine with irreps A_1 , B_1 and B_2 , C_s for pyrimidine with irreps A' and A'').

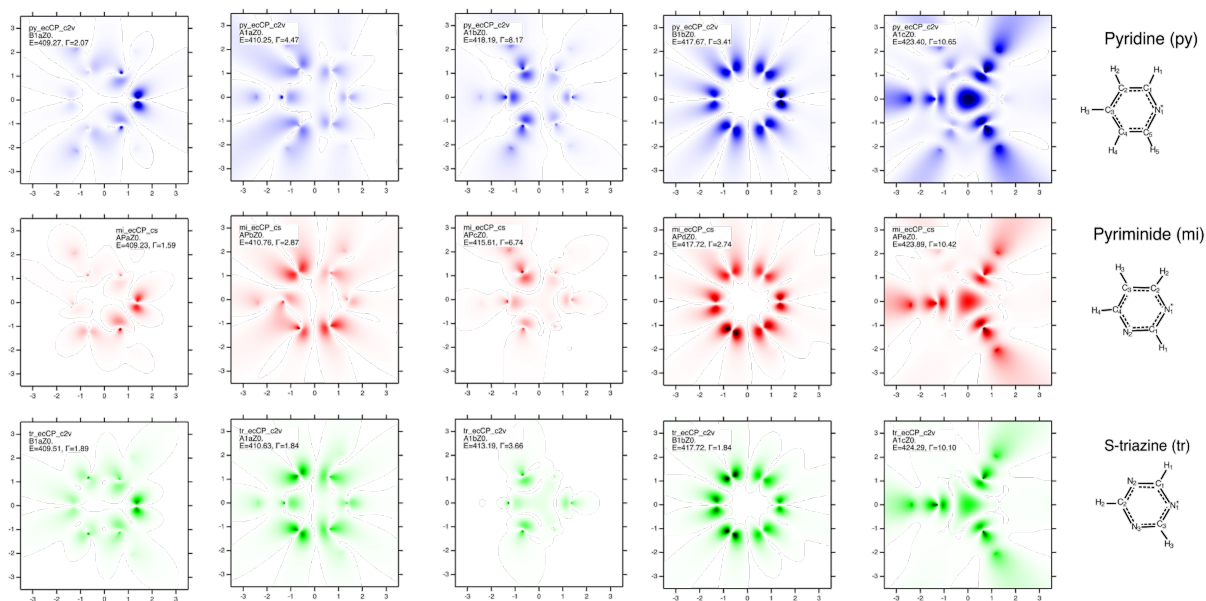


Figure S20: Resonant wave functions (Kapur-Pierls states) of all five resonances of each azabenzene molecule identified in Fig. S19.

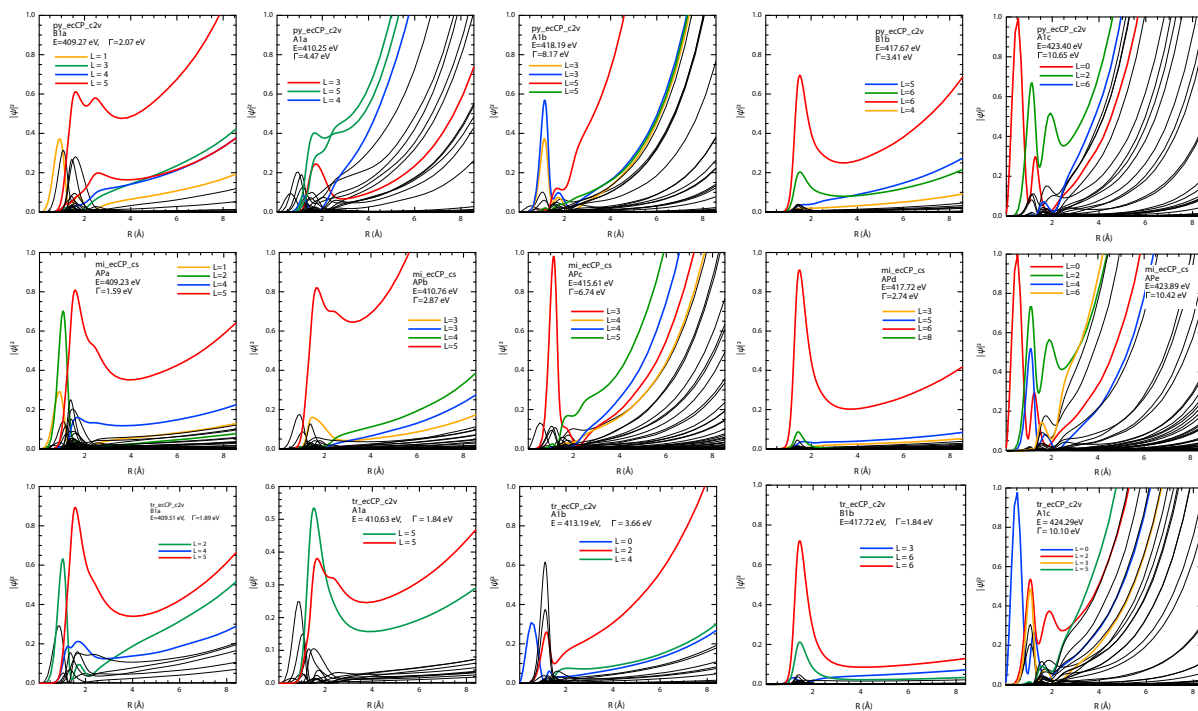


Figure S21: Overview of the radial parts of the partial-wave resonant wave functions (Kapur-Peierls states) of all 5 resonances identified in each of the 3 molecules in Fig. S19. The text in each panel identifies the molecule (top: pyridine, middle: pyrimidine, bottom: *s*-triazine), the irreducible representation, the energy location of the resonance (E) and the width of the resonance (Γ), which can be referenced to Figs. S19 and S20.

4 Additional comparisons between experiment and theory

4.1 Comparison of experimental and theoretical cross sections and asymmetry parameters

This section contains additional comparisons between our experimental measurements and calculations. First, we discuss the comparison of the experimental X-ray absorption cross sections in the vicinity of the nitrogen K-edge from the literature with our calculations. Such a comparison in the case of pyrimidine is shown in Fig. 3 of the main text. Figure S22 shows such comparisons for all three molecules. The experimental cross sections have been taken from Ref. (47). In the case of pyridine (Fig. S22A), the calculations reveal two clear local maxima above the ionization threshold, whereby the location of the lower one quantitatively agrees with the experiment. In the case of pyrimidine (Fig. S22B), both experiment and theory show two clear above-threshold local maxima, the lower of which is in quantitative agreement. The calculated position of the upper maximum is overestimated by ~ 3.5 eV, as discussed and indicated in the main text (Fig. 3). The experimental cross section of *s*-triazine (Fig. S22C) reveals two local maxima, whereas the calculations display three. Based on the shift of ~ 3.5 eV encountered in the case of pyrimidine and the similarity of the two molecules, we propose that the higher-lying observed maximum is assigned to the highest-lying of the three calculated maxima.

The comparison shown in Fig. S22 was also used to determine accurate values of the N-1s ionization energies, which were used for consistency in the remainder of this work. Specifically, the calculated photoionization cross sections were shifted to best match the measured X-ray absorption spectra and these shifts were used to determine the N-1s ionization energies. In this way, we obtained N-1s binding energies of 404.0 eV, 404.3 eV and 404.6 eV for pyridine, pyrimidine and *s*-triazine, respectively. These values are in reasonable agreement with the literature values (47). The overall shifts of the CP (ECO) calculations, that were carried out without initially taking into account the N-1s chemical shifts, thus amounted to 0.9 eV (4.6 eV), 0.6 eV (4.3 eV) and 0.3 eV (4.0 eV). These shifts were applied in all comparisons of experiment and theory shown in this work.

In addition to determining time delays, the present work has also accessed the N-1s photoelectron asymmetry parameters of the azabenzene molecules, which have not been reported in the literature so far. Figure S23 compares the asymmetry parameters (β) measured in this work with the CP and ECO calculations. The β -values are found to increase from close to zero near threshold to values ranging from 1-1.25 around 450 eV. In all three molecules, we find reasonable agreement between the measured and calculated asymmetry parameters and a slightly better agreement for the CP calculations, which further justifies our choice made in the main text to focus the comparisons and discussions on these calculations.

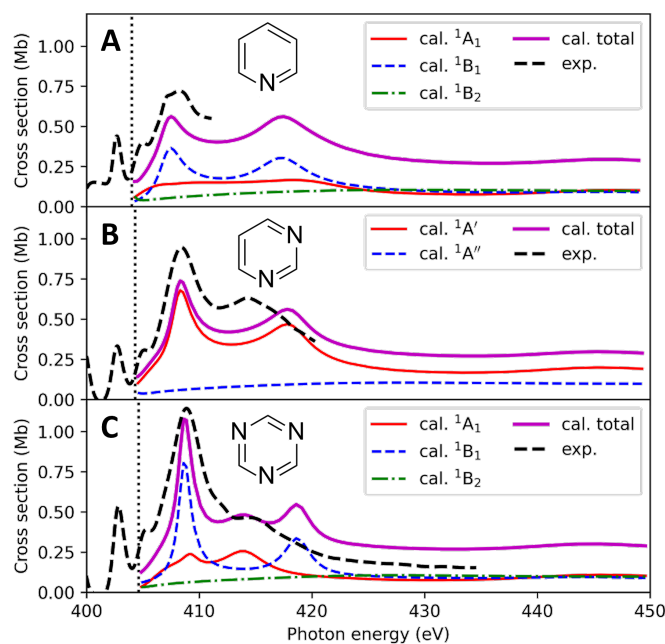


Figure S22: Comparison of experimental (Ref. (47)) and theoretical (this work) photoionization cross sections at the nitrogen K-edge, where the ionization potential is indicated by the vertical dotted line. The full magenta line is the total photoionization cross section, whereas the other colored lines are the symmetry-resolved partial cross sections. The calculations shown in this figure have been shifted to lower energies by 0.9 eV, 0.6 eV and 0.3 eV in the cases of pyridine, pyrimidine and *s*-triazine, respectively, as mentioned in the text.

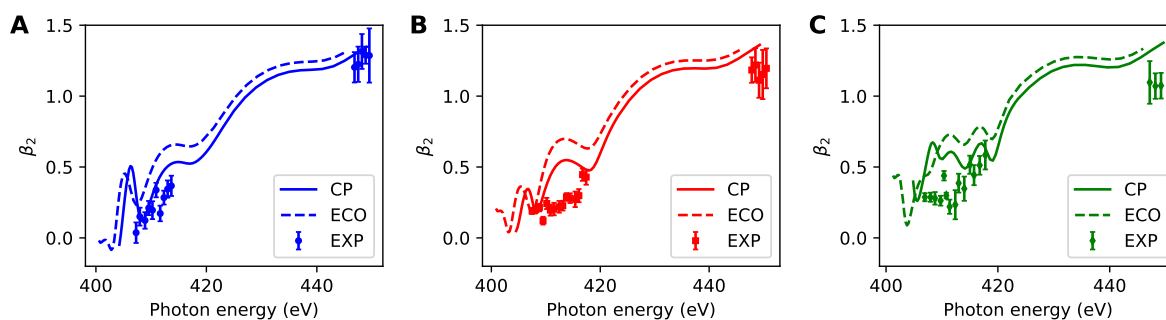


Figure S23: Asymmetry parameters (β_2) of nitrogen 1s electrons of pyridine (A), pyrimidine (B), and *s*-triazine (C), with the correlation-polarization potential (CP) or the equivalent-core orbitals (ECO) calculations compared to the experimental (EXP) values from this work extracted by Abel inversion. The CP calculations have been shifted by the same amount as in Fig. S22 and the ECO calculations have been shifted by an additional 3.7 eV, as mentioned in the text.

4.2 Comparison of Coulomb-laser coupling delays with TDSE and experiments

Next, we discuss the performance of various analytical expressions of the CLC delays, which have been shown to be equivalent to the continuum-continuum delays of RABBIT (3). The most widely used and simplest version consists of only the phase of the hydrogenic continuum-continuum-transition matrix element and is labeled "P" in Refs. (34, 52). A better approximation is obtained by adding correction factors for the long-range amplitudes of the continuum wave functions. This gives rise to the improved "P+A" (for phase+amplitude) version of the CLC delays. A third version of the CLC delays is obtained by moving the starting point of the integration of the radial continuum wave functions away from the origin, which is known as "P+A'" (52). Finally, Serov et al. introduced yet another analytical expression of the CLC delays, which differ from the other ones, notably in depending on the Wigner delays (see Eq.(14.41) in Ref. (53)).

Since the energy grid accessed in our measurements is quite dense (especially compared to RABBIT experiments) and extends to unusually low kinetic energies close to 2 eV, the present data is particularly sensitive to the CLC delays. We first investigate the performance of the different CLC formulae through a direct comparison with the solution of the time-dependent Schrödinger equation (TDSE). Such a comparison is shown in Fig. S24A, which compares the different versions of the CLC delays from Ref. (34), added to the analytically known photoionization delays of the hydrogen atom, with TDSE calculations of attosecond angular streaking of atomic hydrogen ionized by an attosecond short-wavelength pulse (30). This comparison shows that among all available variants of the CLC delays, the best agreement with a TDSE simulation of attosecond angular streaking of the hydrogen atom is achieved by the arithmetic average of the P and P+A delays. This result indicates that this particular form of the CLC delays should be expected to perform best when we compare experiment and theory.

Panels B-F of Fig. S24 show the comparison of the experimental data from this work with the azabenzene delays from the CP calculations to which we added the different variants of the CLC delays. As expected on the basis of the results shown in panel A, we find that the arithmetic average of the P and P+A delays yields the best agreement between theory and experiment. Therefore, we have chosen this approach to describing the CLC delays for the results shown in the main text.

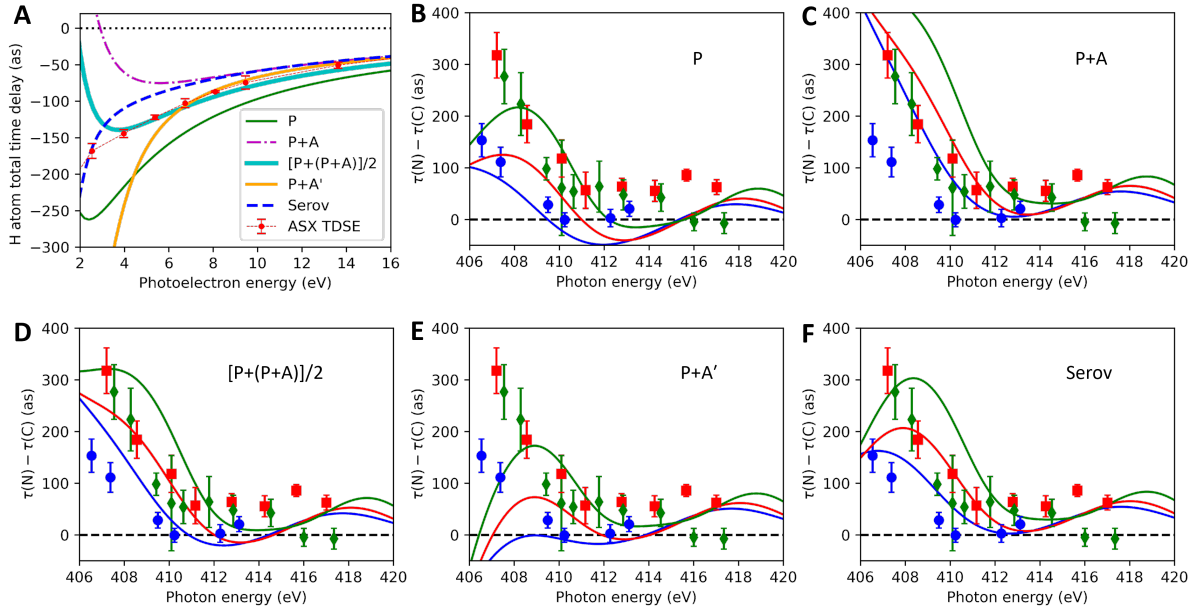


Figure S24: Comparison of different versions of the CLC delays with TDSE and experimental results. The results from TDSE calculations of attosecond angular streaking of atomic hydrogen (“ASX TDSE”) are compared in (A) to the sum of the atomic Wigner delay and the different variants of the CLC delays. “Serov” refers to the expression of the CLC delays given in Eq. (14.41) of Ref. (53). In (B-F) the full lines are the total calculated delays, i.e. a sum of the one-photon-ionization delays calculated with the CP method and the CLC delays calculated according to different CLC formulae, specifically (B) P, (C) P+A, (D) the arithmetic average of P and P+A, (E) P+A’ in Ref. (52), and (F) derived by Serov *et al* (53).

4.3 The role of post-collision interactions

Finally, we discuss the role of the Auger-Meitner (AM) decay and the post-collision interaction (PCI) between the photoelectron and the AM electron. Following N-1s ionization, KVV AM decay creates AM electrons with kinetic energies of ~ 380 eV, which are not detected in our experiments because their momenta are larger than the maximal momentum that is projected on the cVMI detector. The 1s vacancy of nitrogen has an AM lifetime of 5.1 fs (54). The N-1s photoelectron thus initially leaves behind a singly charged molecular cation. Since the AM electron is much faster than the photoelectron, the former will overtake the latter, which then evolves in the long-range potential of a doubly-charged cation. Since a rigorous quantum-mechanical description of the effect of AM decay and PCI on photoionization delays is not yet available and is beyond the scope of this work, we here resort to simple estimations.

First, it is worth recalling that photoionization (Wigner) delays can be decomposed into the sum of a delay originating from the Coulomb potential and a delay originating from the short-range potential (3). Since both the Coulomb delays and the CLC delays are known analytically, we can express the change in these delays from $Z = 1$ to $Z = 2$ analytically. These results are shown in Fig. S25A, which shows the difference between the total photoionization delay (Wigner+CLC) for $Z = 2$ and $Z = 1$ for the different variants of the CLC correction discussed in the previous section. We find that these corrections all agree well above kinetic energies of ~ 10 eV, but diverge at lower kinetic energies.

Next, exploiting the additivity of the short-range, Coulomb and CLC delays, we can "correct" the calculated time-delay results shown in the main text for the occurrence of the PCI effect, i.e. for the switch from $Z = 1$ to $Z = 2$ when the AM electron overtakes the photoelectron. For this purpose, we take the calculated Wigner delays (as shown, e.g. in Fig. 4D,E,F of the main text), add the difference of Coulomb delays for $Z = 2$ and $Z = 1$ ($L = 0$ in both cases for 1s electrons) and add the CLC delay for $Z = 2$. The resulting delays are shown as dashed lines in Fig. S25B-F, together with the results that ignore the PCI effect (from Fig. 3A of the main text) as full lines. The dashed and full lines can thus be viewed as the two limiting cases of an infinite and a vanishing AM lifetime, respectively. For most variants of the CLC delays, the discussed correction is minor, especially for the CLC correction $[P+(P+A)]/2$ (see section 4.2) that best agrees with the TDSE results (Fig. S25D). We therefore conclude that the possible effect of PCI on the measured time delays is minor and can be safely neglected in the interpretation of the present results.

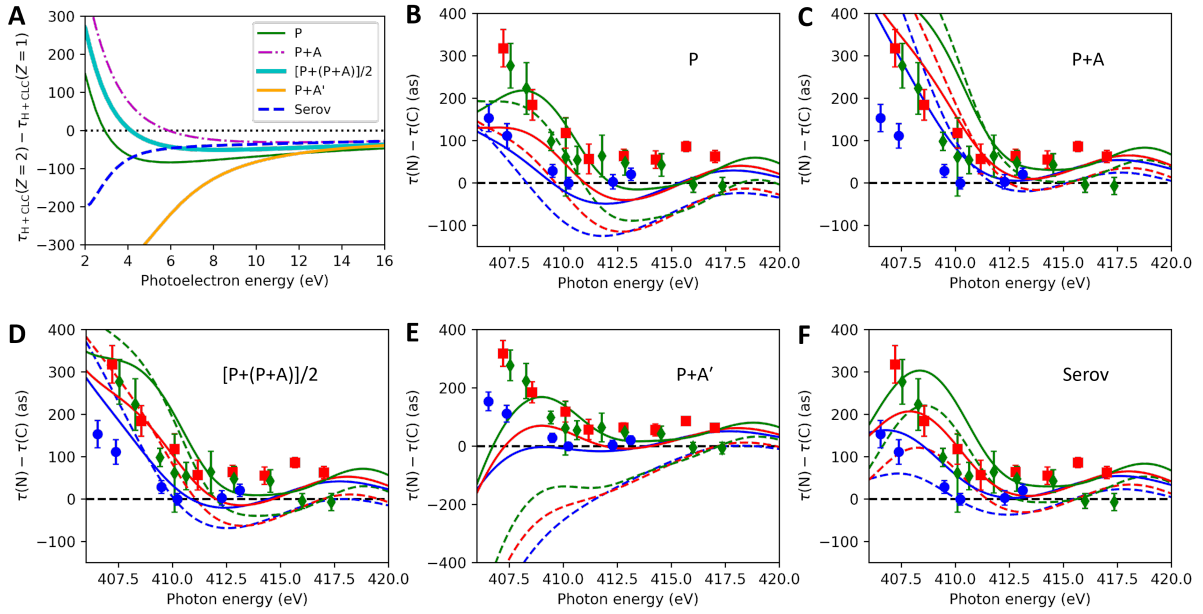


Figure S25: Illustration of the effect of PCI on photoionization delays. A) Difference of the total photoionization delays (Wigner + CLC) for a hydrogenic system with $Z = 2$ vs. $Z = 1$ ($L = 0$ in both cases), i.e. $\tau_{H,Z=2}^{\text{Wigner}} + \tau_{Z=2}^{\text{CLC}} - \tau_{H,Z=1}^{\text{Wigner}} - \tau_{Z=1}^{\text{CLC}}$. B-F) The symbols with error bars are the experimental data and the full lines are the calculations, both reproduced from Fig. 3A of the main text. The dashed lines are obtained from the solid lines as follows: $\tau_{\text{dashed}} = \tau_{\text{solid}} + \tau_{H,Z=2}^{\text{Wigner}} + \tau_{Z=2}^{\text{CLC}} - \tau_{H,Z=1}^{\text{Wigner}} - \tau_{Z=1}^{\text{CLC}}$.

References and Notes

1. M. Schultze, *et al.*, *Science* **328**, 1658 (2010).
2. K. Klünder, *et al.*, *Phys. Rev. Lett.* **106**, 143002 (2011).
3. R. Pazourek, S. Nagele, J. Burgdörfer, *Rev. Mod. Phys.* **87**, 765 (2015).
4. M. Huppert, I. Jordan, D. Baykusheva, A. von Conta, H. J. Wörner, *Phys. Rev. Lett.* **117** (2016).
5. J. Vos, *et al.*, *Science* **360**, 1326 (2018).
6. S. Biswas, *et al.*, *Nat. Phys.* **16**, 778 (2020).
7. A. Kamalov, A. L. Wang, P. H. Bucksbaum, D. J. Haxton, J. P. Cryan, *Physical Review A* **102**, 023118 (2020).
8. S. Nandi, *et al.*, *Science Advances* **6**, eaba7762 (2020).
9. S. Heck, *et al.*, *Science advances* **7**, eabj8121 (2021).
10. X. Gong, *et al.*, *Nature* **609**, 507 (2022).
11. S. Heck, *et al.*, *Physical review letters* **129**, 133002 (2022).
12. I. Jordan, *et al.*, *Science* **369**, 974 (2020).
13. A. L. Cavalieri, *et al.*, *Nature* **449**, 1029 (2007).
14. S. Neppl, *et al.*, *Nature* **517**, 342 (2015).
15. Z. Tao, *et al.*, *Science* **353**, 62 (2016).
16. F. Siek, *et al.*, *Science* **357**, 1274 (2017).
17. J. Duris, *et al.*, *Nature Photonics* **14**, 30 (2020).
18. S. Li, *et al.*, *Optics express* **26**, 4531 (2018).
19. S. Li, *et al.*, *Science* **375**, 285 (2022).
20. Y. Ling, *et al.*, *Drug Design, Development and Therapy* pp. 4289–4338 (2021).
21. T. P. Selvam, C. R. James, P. V. Dniandev, S. K. Valzita, *Research in Pharmacy* **2** (2015).
22. A. Sharma, R. Sheyi, B. G. de la Torre, A. El-Faham, F. Albericio, *Molecules* **26**, 864 (2021).
23. A. Moliton, *Optoelectronics of molecules and polymers*, vol. 104 (Springer, 2010).
24. P. Walter, *et al.*, *Journal of Synchrotron Radiation* **29**, 957 (2022).
25. Z. Zhao, Z. Chang, X. Tong, C. Lin, *Optics express* **13**, 1966 (2005).

26. P. Eckle, *et al.*, *Nature Physics* **4**, 565 (2008).
27. A. Kazansky, A. Bozhevolnov, I. Sazhina, N. Kabachnik, *Physical Review A* **93**, 013407 (2016).
28. A. Kazansky, I. Sazhina, N. Kabachnik, *Optics Express* **27**, 12939 (2019).
29. N. Hartmann, *et al.*, *Nature Photonics* **12**, 215 (2018).
30. A. S. Kheifets, *et al.*, *Physical Review A* **106**, 033106 (2022). Publisher: American Physical Society.
31. V. V. Serov, A. S. Kheifets, *Journal of Physics B: Atomic, Molecular and Optical Physics* **56**, 025601 (2023).
32. J. M. Glowina, *et al.*, *Optics express* **18**, 17620 (2010).
33. M. Piancastelli, *Journal of Electron Spectroscopy and Related Phenomena* **100**, 167 (1999).
34. J. M. Dahlström, A. L'Huillier, A. Maquet, *Journal of Physics B: Atomic, Molecular and Optical Physics* **45**, 183001 (2012).
35. Z. Zhang, *et al.*, *New Journal of Physics* **22**, 083030 (2020).
36. M. Seaberg, *et al.*, *Synchrotron Radiation News* **35**, 20 (2022). Publisher: Taylor & Francis _eprint: <https://doi.org/10.1080/08940886.2022.2066416>.
37. S. Li, *et al.*, *AIP Advances* **8**, 115308 (2018). Publisher: American Institute of Physics.
38. R. Obaid, *et al.*, *Journal of Physics B: Atomic, Molecular and Optical Physics* **51**, 034003 (2018). Publisher: IOP Publishing.
39. M. C. Hettrick, J. H. Underwood, P. J. Batson, M. J. Eckart, *Applied optics* **27**, 200 (1988).
40. A. E. Orel, T. N. Rescigno, B. H. Lengsfeld Iii, *Physical Review A* **42**, 5292 (1990). PRA.
41. F. A. Gianturco, R. R. Lucchese, N. Sanna, *Journal of Chemical Physics* **100**, 6464 (1994).
42. A. P. P. Natalense, R. R. Lucchese, *Journal of Chemical Physics* **111**, 5344 (1999).
43. J. P. Perdew, A. Zunger, *Physical Review B* **23**, 5048 (1981).
44. J. Dunning, Thom H., *Journal of Chemical Physics* **90**, 1007 (1989).
45. C. A. Marante, *et al.*, *Physical Review A* **102**, 012815 (2020). PRA.
46. M. Hoshino, *et al.*, *Journal of Physics B: Atomic, Molecular and Optical Physics* **51**, 065402 (2018).
47. G. Vall-Ilosera, *et al.*, *Journal of Chemical Physics* **128** (2008).
48. R. R. Lucchese, F. A. Gianturco, *International Reviews in Physical Chemistry* **15**, 429 (1996).
49. A. M. Lane, D. Robson, *Physical Review* **151**, 774 (1966). PR.

50. H. D. Meyer, O. Walter, *Journal of Physics B: Atomic and Molecular Physics* **15**, 3647 (1982).
51. V. I. Kukulin, V. M. Krasnopol'sky, J. Horáček, *Theory of Resonances: Principles and Applications* (Springer Netherlands, Dordrecht, 1989).
52. J. M. Dahlström, *et al.*, *Chemical Physics* **414**, 53 (2013).
53. V. V. Serov, V. L. Derbov, T. A. Sergeeva, *Advanced Lasers: Laser Physics and Technology for Applied and Fundamental Science*, O. Shulika, I. Sukhoivanov, eds., Springer Series in Optical Sciences (Springer Netherlands, Dordrecht, 2015), pp. 213–230.
54. C. Nicolas, C. Miron, *Journal of Electron Spectroscopy and Related Phenomena* **185**, 267 (2012).